Energy 310 (2024) 133245

Contents lists available at ScienceDirect

Energy

journal homepage: www.elsevier.com/locate/energy

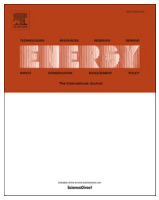

Scaling up magnetocaloric heat pump for building decarbonization initiatives

Jierong Liang [a,b,c,*], Marvin Masche [a], Kun Wang [a,d], Tim Sittig [c], Dimitri Benke [c], Maximilian Fries [c], Kurt Engelbrecht [a,1], Christian R.H. Bahl [a,2]

[a] Department of Energy Conversion and Storage, Technical University of Denmark, Anker Engelunds Vej, 2800, Kgs. Lyngby, Denmark
[b] Section of Thermal Energy, Department of Civil and Mechanical Engineering, Technical University of Denmark, Koppels Allé, 2800, Kgs. Lyngby, Denmark
[c] MagnoTherm Solutions GmbH, Pfungstädter Str. 102, 64297, Darmstadt, Germany
[d] Institute of Microstructure Technology, Karlsruhe Institute of Technology, 76344, Karlsruhe, Germany

ARTICLE INFO

Keywords:
Heat pump
Magnetic regenerator
Building heating
Feedback control
Model predictive control
Magnetocaloric heat pump

ABSTRACT

Building decarbonization necessitates renewable heating and cooling solutions such as heat pumps. Magnetocaloric heat pumps (MCHP) offer environmental and efficiency advantages but face challenges when scaling up from existing active magnetic regenerator configurations. This study highlights uneven flow resistance, porosity, and refrigerant magnetocaloric effects as key obstacles to MCHP performance in parallel multi-bed setups. To address these effects, two control strategies for the fluid flow control system were investigated: measurement feedback control and model predictive control. Results show a 36.9 % heating power improvement with measurement feedback control, though with extended control convergence times. Model predictive control achieved approximately seven times faster control convergence compared to the measurement feedback control strategy, despite exhibiting minor overshooting. Utilization factor-based model predictive control increased the heating capacity by 1.6 %–30.9 % and the COP by 1.2 %–10.7 % in scenarios with uneven flow resistance and porosity, offering computational efficiency but assuming even magnetocaloric effects between regenerators. This assumption can be addressed by outlet temperature-based model predictive control, albeit at a higher computational cost using genetic algorithm. The findings emphasize the importance of advanced control methods to scaling up MCHP in renewable energy building systems.

Nomenclature

Abbreviations	
AMR	Active magnetic regenerator
COP	Coefficient of performance
DSC	Differential scanning calorimetry
MCE	Magnetocaloric effect
MCHP	Magnetocaloric heat pump
MCM	Magnetocaloric material
PV	Photovoltaic
Variables	
A_c	Cross sectional area, [m^2]
a_0	Geometry factor, [−]
Bi	Biot number, [−]
c	Specific heat capacity, [J kg^{-1} K^{-1}]
f	Frequency, [Hz]
H	Internal magnetic field, [A m^{-1}]
h	Convective heat transfer coefficient, [w m^{-2} K^{-1}]
k	Thermal conductivity, [w m^{-1} K^{-1}]
L	Length, [m]
$\dot{m}$	Flow rate, [kg s^{-1}]
n	Effective step length, [−]
NTU	Number of transfer units, [−]
p	Pressure, [Pa]
R	Flow resistance, [Pa s m^{-1}]
s	Specific entropy, [J K^{-1} kg^{-1}]
T	Temperature, [K]
t	Time, [s]
U	Utilization, [−]
$\dot{V}$	Velocity, [m s^{-1}]

(continued on next column)

(continued)

(continued on next page)

* Corresponding author. Department of Energy Conversion and Storage, Technical University of Denmark, Anker Engelunds Vej, 2800, Kgs. Lyngby, Denmark.
E-mail address: jilia@dtu.dk (J. Liang).
[1] presently at Viegand Maagøe A/S, Nørre Søgade 35, 1370 Copenhagen, Denmark.
[2] Presently at: Subra A/S, Bygmarken 4, 3520 Farum, Denmark.

https://doi.org/10.1016/j.energy.2024.133245
Received 17 June 2024; Received in revised form 21 August 2024; Accepted 20 September 2024
Available online 23 September 2024

(*continued*)

x	Axial position coordinate [m] or arbitrary variable
z	z-score, [−]
Greek symbols	
a	Specific surface area, [m^{-2}]
γ	Relative flow resistance, [−]
Δ	Difference
ϵ	Porosity, [−]
θ	Solenoid valve opening period in degree, [°]
ρ	Density, [kg m^{-3}]
τ	Period time, [s]
φ	Penalty function parameter, [−]
ϕ	Rotational angle in degree, [°]
ψ	Binary variable for solenoid valve status, [−]
ω	Center position of solenoid valve opening period, [°]
Subscripts	
avg	Average
c	Cold side
close	Closed state
f	Fluid
h	Hot side
in	Inlet
open	Open state
out	Outlet
pump	Pump
s	Solid

1. Introduction

The acceleration of global energy consumption within the building sector has been conspicuous over the past century, propelled by factors such as population expansion, prolonged indoor activities, and heightened requisites for building functionalities. Eurostat data underscores this trend, indicating that approximately 50 % of the total energy utilized in the EU is allocated for heating and cooling purposes, with fossil fuels, primarily natural gas, accounting for over 70 % of this consumption [1]. In the residential domain specifically, roughly 80 % of final energy consumption is attributed to space and water heating. Aligned with the objectives outlined in the REPowerEU plan [2], which aims to curtail fossil fuel dependencies, augment the adoption rate of heat pumps in buildings, and accelerate the implementation of expansive district heating and cooling networks, significant initiatives have been proposed. With a notable surge of 3 million heat pump units installed in 2022 alone, the ambition is to further deploy at least 10 million additional heat pumps by 2027.

Heat pumps present a compelling solution in the field of cooling and heating technology, offering significant potential to further the European Commission's goals of transitioning towards a carbon-neutral Europe through renewable energy initiatives. Their versatility allows for the provision of renewable cooling, space heating, and hot water, presenting a flexible alternative to conventional fossil fuel-based methods. Concurrently, as the scientific community directs its focus towards buildings equipped with renewable energy systems and low-carbon technologies, there has been a concerted effort to explore new refrigerants [3] and investigate alternative refrigeration technologies [4–7]. Among these, caloric heating and cooling has emerged as a promising refrigeration technology [8–10], incorporating magnetocaloric [11,12], elastocaloric [13–15], barocaloric/mechanocaloric [16–18], and electrocaloric [19–21] approaches. Notable progress in caloric cooling and heating prototypes is documented in Refs. [22–26].

In the RES4BUILD project [27], a magnetocaloric heat pump (MCHP) is integrated in a renewable energy-based system, aiming to decarbonize building energy consumption (Fig. 1). This system, tailored to individual building and climate conditions, features a novel multi-source heat pump concept. It incorporates the MCHP coupled with the evaporator of a two-stage vapor compression heat pump. Additionally, other innovative technologies such as photovoltaic (PV) cells, solar thermal energy collectors, and energy piles [28] will be customized to suit each building's requirements. To support the decarbonization of building energy consumption, PV thermal systems provide renewable heating and cooling solutions [29]. However, while magnetocaloric heat pumps (MCHPs) offer benefits such as zero gaseous refrigerant emissions and reduced noise, they are not yet commercialized, unlike magnetocaloric refrigerators, which are in the very early stages of commercialization. The state-of-the-art MCHP system, utilizing the magnetocaloric effect (MCE), comprises an active magnetic regenerator (AMR) assembly, a magnetic circuit for field variation, and a synchronized hydraulic system [30]. As a pivotal MCHP component, the AMR undergoes crucial operations: adiabatic magnetization, fluid flow from cold to hot reservoir, adiabatic demagnetization, and reversed flow from hot to cold reservoir.

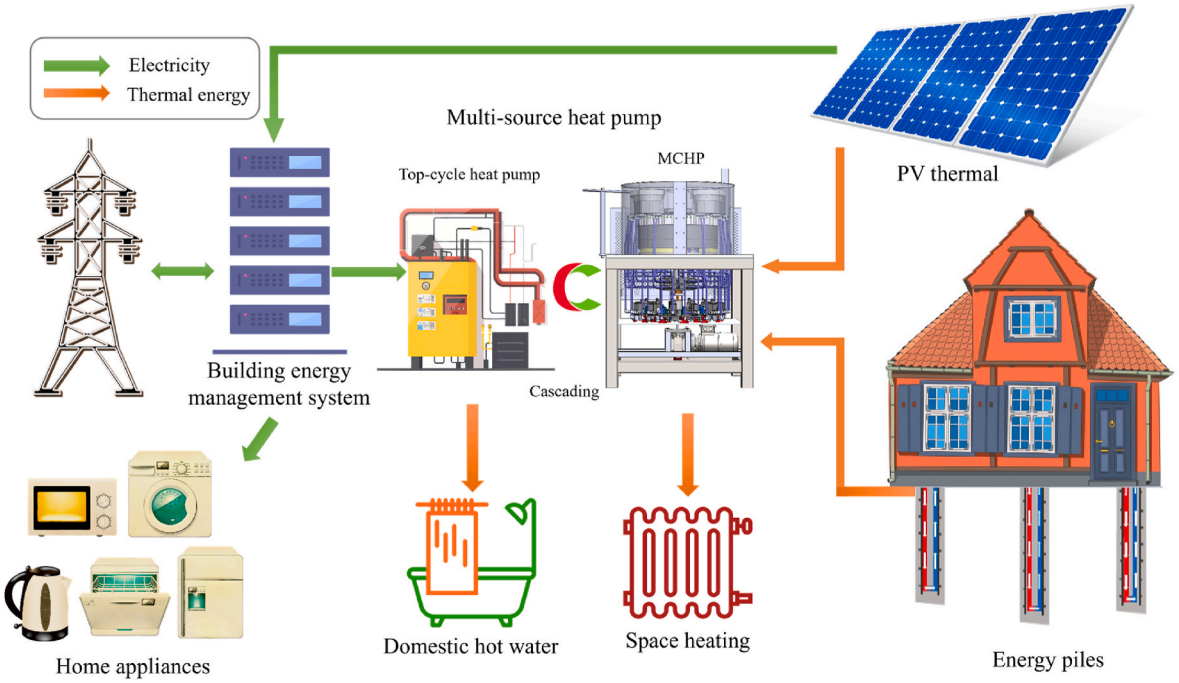

Fig. 1. Schematic of a MCHP integrated in a in a renewable energy-based building system.

AMRs function as integrated units for heat exchange and heat generation, while the heat transfer fluid directly connects the thermodynamic cycles in question, and the heat capacity of the magnetocaloric material (MCM) is used as a regenerator to transfer the heat from a neighboring cycle. The key advantage of AMR configuration lies in achieving temperature spans significantly surpassing adiabatic temperature change of MCMs (solid refrigerants) [31,32]. Through sequential magnetic field variations and fluid flow steps, the AMR efficiently transfers cooling capacity from the cold reservoir while rejecting heat to the hot reservoir over a temperature span, requiring mechanical, magnetic, electronic, and hydraulic power inputs. Over 80 room temperature magnetocaloric devices have been documented, with a predominant focus on refrigeration than heat pumping [33–35]. These devices explore two primary configurations based on the movement of MCM within a magnetic field: (a) Reciprocating [36], where the AMR reciprocates in and out of the magnetic field using dual magnetic field sources for continuous cooling; (b) Rotary [37], wherein the AMR rotates and traverses a circular path in and out of the field, with fluid flow categorized as axial [38], radial [39], and azimuthal [40]. The rotation of the magnetic field source over static AMR is a prevalent technique in recent prototypes [30].

As an alternative to vapor compression heat pumps, MCHP offers significant environmental benefits primarily through energy savings during regular operation, outweighing concerns about direct emissions from gaseous refrigerants [41]. The concept of low exergy building systems [42,43] introduces new possibilities for low-temperature lift heat pumps (as low as 10 K) with ultra-high COP, a favorable scenario for MCHP due to the reversible but relatively low MCE with current stable MCMs. However, achieving the required heating capacity of at least 1 kW for the building system necessitates scaling up MCHP with multi-bed AMRs, which can be hydraulically connected in series or parallel. Serially connected devices, typically comprising two AMR beds sharing a common cold reservoir with flow provided by reciprocating displacers, offer advantages such as balanced flow in each bed and flow calculation based on displacer geometry [44–46]. Conversely, parallelly connected AMR beds feature a fluid circulator with constant unidirectional flow connected to a set of flow manifolds [47–49]. Here, individual AMR beds are hydraulically connected in parallel via flow manifolds, and flow to each bed is controlled by valves. The advantages of a parallel flow circuit include a more compact system and less expensive construction due to better magnetic field utilization. However, parallel connections between beds may result in unequal flow distribution, leading to unbalanced fluid flow and reduced AMR performance [50].

Inspired by research on optimizing the timing and synchronization between magnetic circuit and fluid flow profiles to enable diverse thermodynamic cycles, controlling the operation of each individual AMR in a parallel multi-bed MCHP involves understanding the interplay between AMR performance and magnetic and fluid flow waveforms. There is a consensus in the literature that optimizing cooling capacity involves displacing fluid during periods of extreme magnetic field values with minimized transition times between high and low levels [51,52]. This allows for flexibility in synchronizing the flow rate profile with the magnetic field profile, ranging from center-aligned to end-aligned, or anywhere in between, yielding competitive performance [53]. Center alignment ensures sufficient temperature difference between solid and fluid at low blow fractions, while end alignment prevents fluid flow during magnetic field reversal, crucial at high blow fractions [54]. Increasing the time delay between magnetization and fluid displacement enables fluid flow to coincide with different magnetic profile stages, resulting in diverse thermodynamic cycles with varying performance trends. Li et al. [55] studied the cooling performance of an AMR under various process time lengths, utilization factors, and operating frequencies, revealing a larger temperature span with longer flow times, albeit with increased motor workload due to intermittent motion. The reported temperature span increases with decreasing blow fraction at a low utilization factor due to increased heat transfer potential [56]. At moderate utilization, AMR performance degradation occurs at low blow fraction due to reduced regenerator thermal effectiveness with NTU [57]. For constant utilization factor, shorter blows typically yield higher temperature span at a given cooling load due to higher average magnetic field during the cold blow, whereas longer blows lead to higher COP for the required temperature span [58,59].

The aforementioned underscores the crucial role of hydraulic circuit parameters, including utilization factor, blow fraction, and magnetic field - fluid flow synchronization, on the cooling capacity and temperature span achieved by AMRs. These insights offer opportunities for effectively managing hydraulics for each individual AMR to scale up MCHP with parallel multi-bed configuration. Fluid flow profiles can be practically adjusted without hardware modifications, given a reliable valving system is in place. A controllable valving system, including rotary valves [60,61], solenoid valves [62–64], or cam valves [56,57], is essential for hydraulic flow management. In parallel multi-bed MCHP, flow imbalance occurs not only due to flow maldistribution among AMRs operating at the same phasing (inter-AMR flow unbalance) but also due to differing displaced volumes between cold and hot blows within the same AMR (intra-AMR flow unbalance). Eriksen et al. [50] adjusted fluid flow through each AMR by tuning additional adjustment valves in each AMR flow channel to mitigate inter-AMR flow imbalances. However, manual control of the opening angle for each adjustment valve, based on average operating conditions, limited adaptation to varying conditions and intra-AMR flow imbalances. Lionte et al. [65] addressed intra-AMR flow imbalances by introducing a small bypass flow from the cold side to the hot side of the AMR using a bypass heat exchanger. Although this increased cooling capacity by 8 %–22 %, implementing individual bypasses for each AMR in a multi-bed configuration made the hydraulic system complex and impractical. A real-time controlled and programmable solenoid valve system was developed to produce well-synchronized fluid flow [66], offering the potential to individually regulate fluid flow of each AMR in a parallel multi-bed MCHP. However, there is a lack of discussion on scaling up a parallel multi-bed MCHP with effective hydraulic control.

This study aims to address the challenges of advancing scaled-up MCHPs integrated in low-carbon building systems. A full-scale MCHP prototype with 13 parallel gadolinium AMR beds was constructed, and a computer-controlled solenoid valving system was developed to address both inter-AMR flow imbalances and intra-AMR flow imbalances in real time. Control of the displaced volume of fluid for each AMR and each blow is achieved by tuning the local blow fraction through adjusting the opening timing of each solenoid valve, without the need for additional components. Different measurement-feedback control strategies, including AMR cold outlet temperature, AMR hot outlet temperature, and both as control feedback parameters, are explored to understand the trade-off between multi-bed operation controllability and device economics. In preparation for future digital twin control with possible rapid control, a detailed numerical model was developed to generate designer maps for simultaneous initial solenoid valve timing as a function of operational variations. Given the limited application of MCHPs in building heating due to their early stage of development, this study addresses the research gap by exploring practical control strategies in a full-scale prototype. These measurement-feedback control and model predictive control strategies provide an effective tool for scaling up MCHPs with parallel multi-bed configurations.

2. Methods

To evaluate the effectiveness of scaled-up MCHP operation, the Technical University of Denmark (DTU) has built a full-scale parallel multi-bed MCHP prototype named MagQueen. This prototype aims to test various measurement-feedback control strategies and validates a numerical model for model predictive control strategies. The model not only incorporates the energy and mass governing equations within a single AMR but also considers different flow resistances and operating

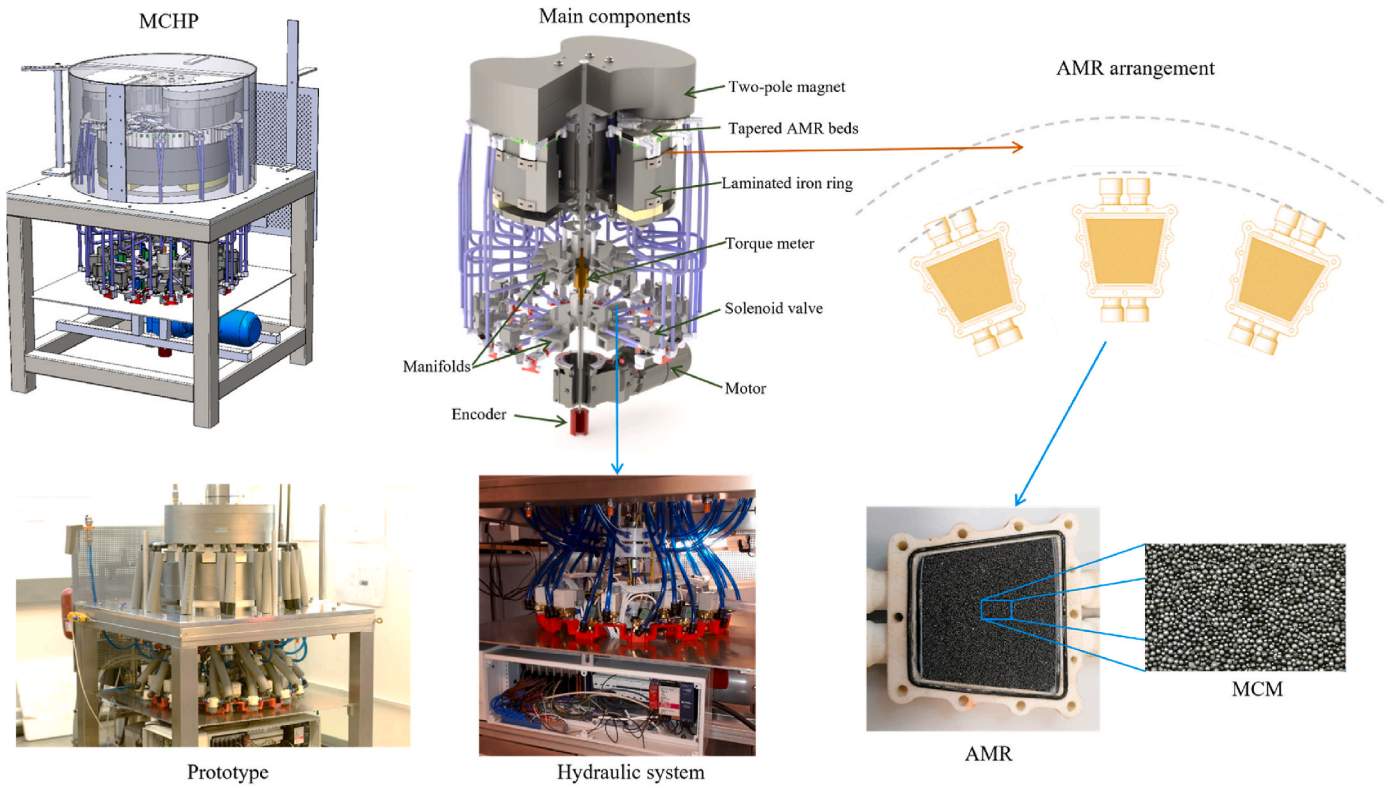

Fig. 2. Illustration of the MCHP prototype.

phases between AMRs. A twofold approach was investigated: (1) measurement-feedback control strategies, encompassing cold-out to hot-out adjustment, biggest outlier seeking, and symmetric adjustment, and (2) model predictive control strategies, including the identical utilization factor method and the identical outlet temperature method.

2.1. Full-scale prototype

The MagQueen, detailed in Ref. [67], was initially engineered to meet the heating demands of a low-energy single-family house in Denmark, offering a superior COP compared to conventional systems. Fig. 2 illustrates the schematic of MagQueen along with its primary design characteristics. The prototype features a rotary two-pole permanent magnet with a maximum flux density of 1.46 T. Thirteen static trapezoid-shaped AMR beds are positioned on top of each iron tooth, a distinctive feature of the solid iron ring with thin laminations and insulation in between to prevent eddy current losses. The magnet design employs iron to concentrate the magnetic flux from the yoke through each AMR bed. The entire fluid flow system includes solenoid valves, a pump, check valves, and manifolds, enabling continuous circulation of the heat transfer fluid throughout the system while facilitating reciprocating flow in each individual AMR bed.

The AMRs in this study are filled with pure gadolinium (Gd) particles as MCMs, each undergoing a magnetic thermodynamic cycle during continuous magnetization and demagnetization. The MCMs act as both heat storage heat exchanger and being heated and cooled by the ramping-up and ramping-down magnetic field, respectively. As the MCM is magnetized, heat transfer fluid is pumped through the AMR bed in the cold-to-hot direction, transferring heat from the MCM to the heat transfer fluid, and vice versa during demagnetization. Notably, fluid flow through the AMRs is reciprocating, while the flow outside AMRs is unidirectional. Approximately 4.4 kg of Gd was used for the entire prototype, with a particle size range of 400–700 μm and an average particle size of 500 μm. The complete flow diagram is illustrated in Fig. 3. The prototype is equipped with 13 high-pressure and 13 low-pressure fast-responding solenoid valves, along with 26 low-pressure drop check valves. For each AMR, two solenoid valves and two check valves are utilized to regulate the flow. These check valves ensure unidirectional fluid flow. The electromechanically operated solenoid valves enable remote control of fluid flow through each regenerator, synchronized with the magnetic field. This allows for precise regulation of the fraction of the cycle when fluid flows through each regenerator in a specific direction. With the ability to independently regulate the valves, each AMR can have a different flow profile, facilitating blow fraction control for each AMR.

As essential control parameters, 26 E-type thermocouples were positioned at both the cold-out and hot-out of each AMR. A torque meter on the magnet shaft measured the power required for magnetic circuit rotation. An absolute rotary encoder on the shaft tracked the magnet angular position, guiding the timing for solenoid valve operation. Flow rate was gauged with both low (0.5–10 L/min) and high (5.7–56.8 L/min) range flow meters.

The flow resistance of each individual AMR was evaluated during both the cold-to-hot and hot-to-cold blows to gauge the extent of flow imbalance and generate parameters for the numerical model. Flow resistance is quantified as the pressure drop across the AMR bed divided by the volumetric flow rate. Using manual control of solenoid valves and the pump while the magnet remains stationary, pressure drop and flow rate are measured by the pressure transducers and a flow sensor, respectively.

The relative combined standard uncertainties were evaluated using the Taylor Series Method (TSM) [68]. Magnetic power uncertainty only considered system uncertainty, attributed to fluctuations from internal AMR operation rather than random errors [69,70]. Notably, relative standard uncertainties estimated for temperature, flow resistance, magnetic work and pumping work, cooling and heating capacities, and COP are 1 %, 2 %, 3 %, 10 %, and 10 %, respectively [39]. Each test condition employed a sampling frequency of approximately 6 Hz, with performance data averaged over a 10-min period upon reaching steady-state conditions.

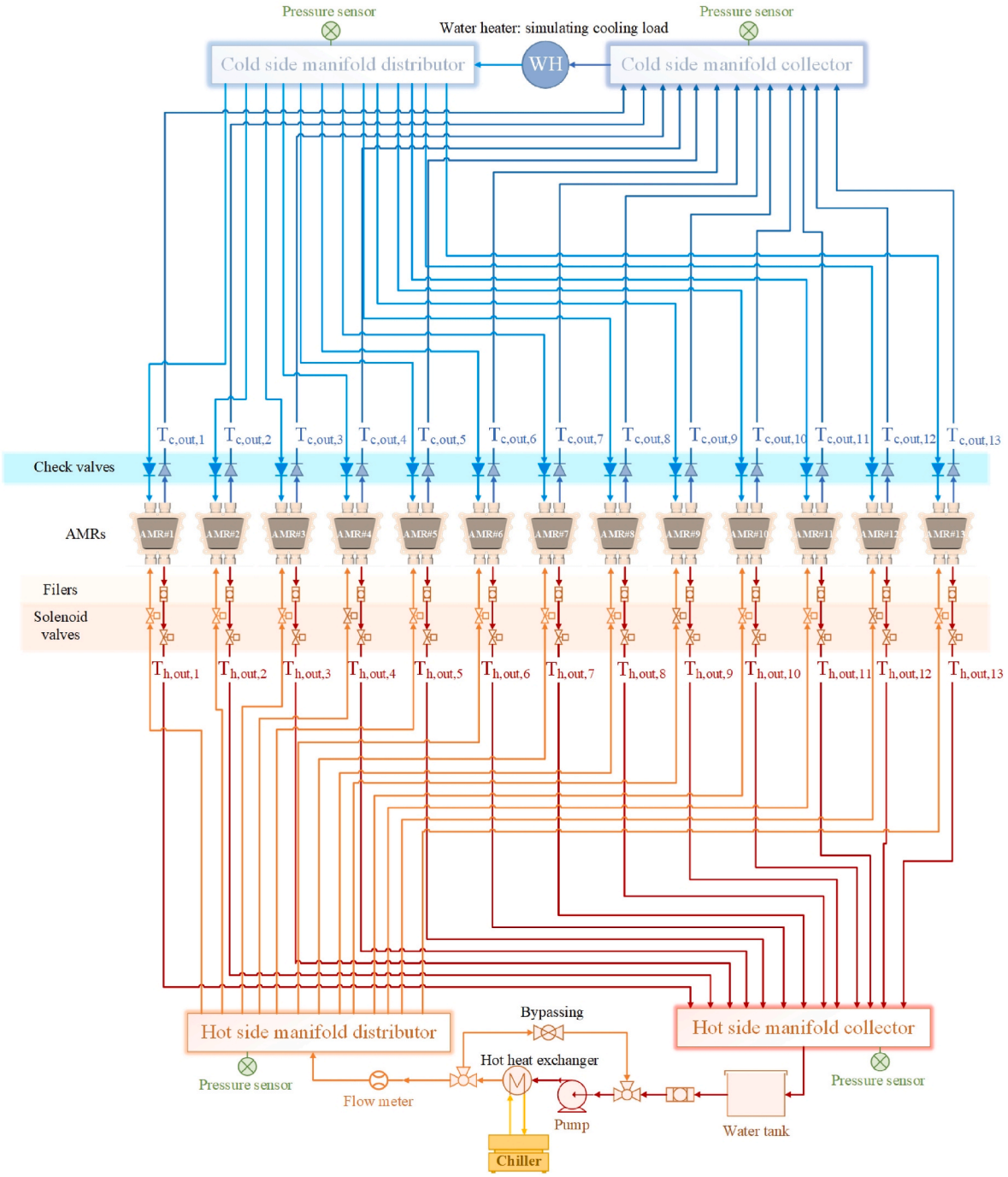

Fig. 3. Flow diagram of the hydraulic system in the MCHP. 'WH' stands for water heater. $T_{c,out,i}$ and $T_{h,out,i}$ denote the cold-out and hot-out temperatures in the ith AMR.

2.2. Measurement feedback control strategies

The proposed measurement feedback control strategies utilize the modified z-score of AMR outlet temperatures as control feedback parameters, as described in Eq. (1). Real-time measurements from thermocouples monitor the AMR outlet temperatures, providing data for z-score calculations. Based on the deviation from the desired setpoint and the derived z-score values, the controller adjusts the control inputs to steer the system towards a desired state. These control inputs may involve altering the opening periods of solenoid valves during hot-to-cold or cold-to-hot blows, depending on the selected strategy.

$$z_i = \frac{x_i - \frac{\sum_{j=1}^{n} x_j|_{j\neq i}}{n-1}}{\sqrt{\frac{1}{n-1}\sum_{k=1}^{n}\left[x_k - \frac{\sum_{j=1}^{n} x_j|_{j\neq i}}{n-1}\right]^2\Big|_{k\neq i}}} \tag{1}$$

In calculating the modified z-score z_i for the ith data point (x_i), the mean and standard deviation of the dataset are computed excluding the ith data point to mitigate the influence of significantly large outliers on the calculations.

For AMR outlet temperatures identified as outliers and exceeding the average temperature, the corresponding solenoid valve opening period

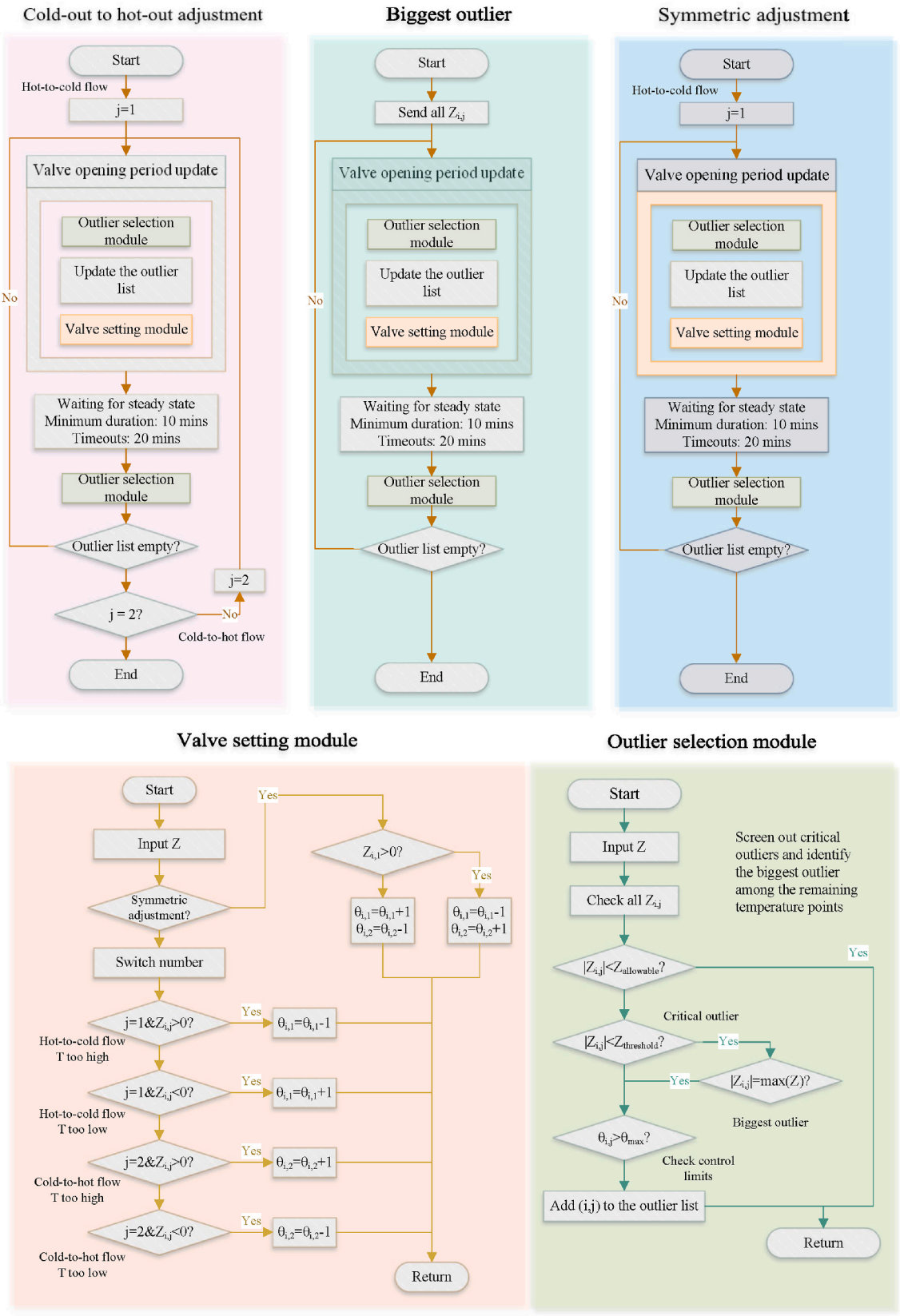

Fig. 4. Control logic diagrams for measurement feedback control, including cold-out to hot-out adjustment, biggest outlier seeking, and symmetric adjustment. The valve setting module and outlier selection module serve as common subfunctions. In the valve setting module, the solenoid valve opening period ($\theta_{i,j}$) increases by +1 when the corresponding AMR cold-out temperature is too low or the hot-out temperature is too high, and vice versa. Specifically, in the symmetric adjustment mode, only the hot-to-cold solenoid valve opening period is adjusted in response to the cold-out temperature, while the cold-to-hot solenoid valve opening period is simultaneously adjusted by the same degree but in the opposite direction. In the outlier selection module, current outliers include all points with z-scores exceeding the predefined threshold value and the point with the highest z-score among the remaining points.

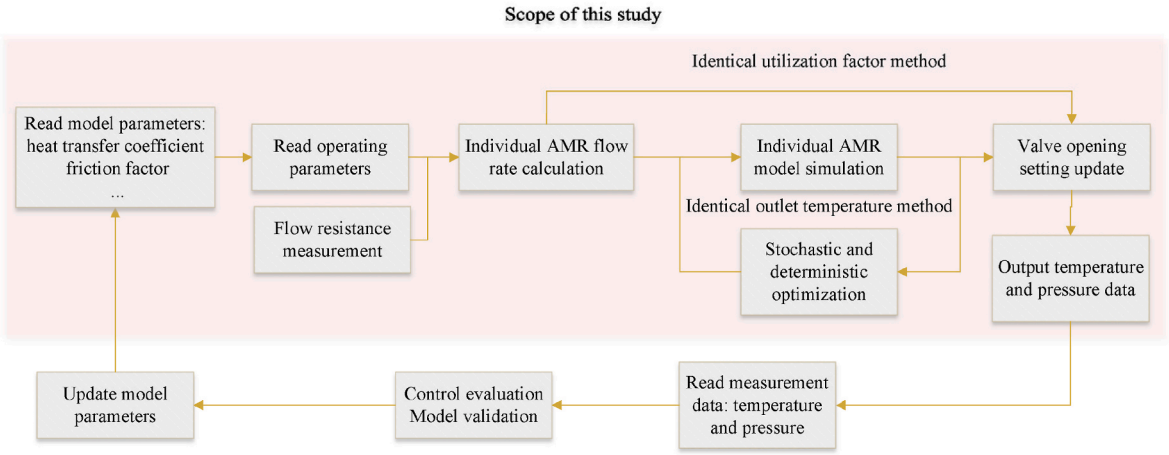

Fig. 5. Schema of model predictive control.

increases, and vice versa. The opening period of the solenoid valve is quantified by the phase angle corresponding to the encoder phase angle. For instance, a phase angle of 60° corresponds to a solenoid valve opening period of 60/360 of the cycle period. Three distinct control strategies are explored, as depicted in Fig. 4.

1. Cold-out to hot-out adjustment: The controller targets the largest outlier from AMR cold-out temperatures, adjusting the corresponding solenoid valve opening period by +1/-1° until no outliers remain. Subsequently, the same process is applied to address outliers in AMR hot-out temperatures.
2. Biggest outlier seeking: The controller identifies the largest z-score value from both AMR cold-out and hot-out temperatures and adjusts the corresponding solenoid valve opening period by +1/-1°. This adjustment continues iteratively until no further outliers are detected. Unless the z-score values exceed the predefined threshold value, this strategy only adjusts one solenoid valve per step due to the strong interdependence between different AMRs.
3. Symmetric adjustment: The controller identifies the largest outlier from AMR cold-out temperatures and adjusts the corresponding solenoid valve opening period by +1/-1°. Simultaneously, it adjusts the opening period of the other solenoid valve at the same AMR by −1/+1° until no outliers are present in the AMR cold-out temperatures. This strategy adjusts the opening periods of two conjugated solenoid valves simultaneously, minimizing the need for thermocouples to monitor AMR hot-out temperatures. However, it does not evaluate outliers in AMR hot-out temperatures, making it less suitable for AMRs with significantly different flow resistances between hot-to-cold and cold-to-hot blows, which is uncommon in typical AMRs.

2.3. Numerical model

The AMR model is structured around energy and mass governing equations derived from a pre-existing 1D model [71,72]. This framework encompasses the MCE, heat transfer, and momentum flow for both solid and fluid phases.

$$\underbrace{A_c(1-\epsilon)\rho_s T_s\left(\frac{\partial s_s}{\partial H}\right)_{T_s}\frac{\partial H}{\partial t}}_{\text{Magnetocaloric heat}}=\underbrace{\frac{\partial}{\partial x}\left(k_{stat}A_c\frac{\partial T_s}{\partial x}\right)}_{\text{Heat conduction}}+\underbrace{h^* aA_c(T_f-T_s)}_{\text{Heat convection}}-\underbrace{A_c(1-\epsilon)\rho_s c_s\frac{\partial T_s}{\partial t}}_{\text{MCM heat storage}} \tag{2}$$

$$\underbrace{h^* aA_c(T_f-T_s)}_{\text{Heat convection}}=\underbrace{\frac{\partial}{\partial x}\left(k_{disp}A_c\frac{\partial T_f}{\partial x}\right)}_{\text{Heat conduction}}-\underbrace{\dot{m}_f c_f\frac{\partial T_f}{\partial x}}_{\text{Heat advection}}+\underbrace{\left|\frac{\partial p}{\partial x}\frac{\dot{m}_f}{\rho_f}\right|}_{\text{Viscous dissipation}}-\underbrace{A_c\epsilon\rho_f c_f\frac{\partial T_f}{\partial t}}_{\text{Heat storage}} \tag{3}$$

where T, p, A_c, $\dot{m}$, ρ, c, ϵ, a, s, and H denote temperature, pressure, cross-sectional area, fluid mass flow rate, density, specific heat, porosity, specific surface area, entropy, and internal magnetic field, respectively. Subscripts f and s indicate fluid and solid phases, respectively. The static conductivity (k_{stat}) and fluid dispersion (k_{disp}) conductivity account for the static 3-D conduction and axial dispersion effect in the porous bed, as described elsewhere [73]. h^* represents the modified conjugate heat transfer coefficient, obtained from empirical correlations, following recommendations in Refs. [31,74].

$$h^* = \frac{h_0}{1+\varkappa \bullet \mathrm{Bi}/a_0} \tag{4}$$

where h_0 represents the heat transfer coefficient, excluding the effects of transverse thermal conductivity and temperature distribution within the solid phase. Bi denotes the Biot number. The geometry factor a_0 is typically constant, for example, $a_0 = 5$ for packed spheres. The expression of $\varkappa$ can be found in Refs. [31,74].

To describe the inter- and intra-AMR flow imbalances in the MCHP model with thirteen-bed AMRs, the flow system model is executed beforehand to generate inputs for each AMR model. The flow resistance ($R_{i,j}$) is defined as the ratio of pressure drop across the ith AMR ($\Delta p_{i,j}$) to the local volumetric flow rate ($\dot{V}$) of the fluid passing through it. The $R_{i,j}$ is determined for each AMR from pressure drop measurements during both hot-to-cold flow ($j = 1$) and cold-to-hot flow ($j = 2$) at various volumetric fluid flow rates. To facilitate the calculation of fluid flow rate distribution, the relative flow rate resistance ($\gamma_{i,j}$) is defined in Eq. (6).

$$R_{i,j} = \frac{\Delta p_{i,j}}{\dot{V}} \tag{5}$$

$$\gamma_{i,j} = \frac{R_{i,j}}{\frac{1}{13}\sum_{i'=1}^{13} R_{i',j}} \tag{6}$$

Note that the flow resistance in this study encompasses the resistances of an AMR bed, a check valve, a solenoid valve, a strainer, and the connecting hoses and fittings. To determine the local fluid flow rate of each AMR, the parameter ψ is introduced as a function of the rotational angle (ϕ) to indicate the corresponding open and close status.

$$\dot{m}_{i,j} = \dot{m}_{pump} \frac{\psi_{i,j}\gamma_{i,j}}{\sum_{i=1}^{13}\left(\psi_{i,j}\gamma_{i,j}\right)} \tag{7}$$

$$\psi_{i,j}(\phi) = \begin{cases} 1, \phi \in \left[\omega_{i,j} - \theta_{i,j}/2, \omega_{i,j} + \theta_{i,j}/2\right] \\ 0, \phi \notin \left[\omega_{i,j} - \theta_{i,j}/2, \omega_{i,j} + \theta_{i,j}/2\right] \end{cases} \tag{8}$$

where $\omega_{i,j}$ and $\theta_{i,j}$ denote the center position of the solenoid valve opening period of the ith AMR and the opening period of the solenoid valve corresponding to the ith AMR during the hot-to-cold flow ($j = 1$) and cold-to-hot flow ($j = 2$), respectively. The values of $\psi_{i,j}(\phi)$ at 1 and 0 indicate the open and close status of the corresponding solenoid valves as a function of the current magnet rotational angle ϕ.

The solenoid valve opening period $\theta_{i,j}$ is defined as the valve opening time, expressed in degrees, relative to the motor rotation period. The motor rotation period corresponds to 360° and is twice the AMR cycle period due to the characteristics of the two-pole magnet assembly.

$$\theta_{i,j} = 360 \bullet \frac{\left(t_{close,i,j} - t_{open,i,j}\right) \bullet f}{2} \tag{9}$$

where f, $t_{open,i,j}$, and $t_{close,i,j}$ denote the AMR frequency, as well as the opening and closing times at the ith AMR during the hot-to-cold flow ($j = 1$) and cold-to-hot flow ($j = 2$), respectively.

The steady-state operation of the MCHP can be solved by utilizing the flow profile for each AMR ($\dot{m}_{i,j}$) as the input parameters for the AMR model. Note that the influence of temperature on fluid viscosity is neglected when determining the flow profile ($\dot{m}_{i,j}$).

2.4. Concept of model predictive control

Model predictive control involves multiple solenoid valve adjustments based on a single model prediction, enabling the simultaneous update of all solenoid valve settings in one control step. Given the complex relationship between the variables from different AMRs, utilizing model predictions to adjust the valve settings in response to operational changes can expedite control convergence. As shown in Fig. 5, the model prediction is evaluated and refined on the fly through the framework of digital twins. The concept of digital twins bridges the gap between the digital technologies and analogous world, offering applications in optimizing heat pump operations [75]. Digital twins that continuously update parameters using measured data can yield high-precision short-term predictions. After adjusting parameters with real-time monitoring data, the digital twin model provides more accurate predictions, reducing discrepancies between model estimates and final solenoid valve settings. As an initial step, this study focuses on the effectiveness of two model predictive control methods through one control step, without connecting the simulation to measurements. The impact of parameter updates through iterative measurements will be explored in future studies. The identical utilization factor method and identical outlet temperature method are defined below, with the even valve setting mode as the baseline. In the even valve setting mode, the solenoid valve opening periods are identical for either the hot-to-cold flow direction ($\theta_{i,1}$) or the cold-to-hot flow direction ($\theta_{i,2}$), although the values of $\theta_{i,1}$ and $\theta_{i,2}$ can differ.

1. Identical utilization factor method: The controller estimates the opening period of the solenoid valve assuming an identical utilization factor for each AMR. Considering the mass flow rate variations resulting from diverse flow resistance values between AMRs (Eq. (6)), the solenoid valve opening period ($\theta_{i,j}$) can be determined by solving the following equation equating local utilization factor of each AMR ($U_{i,j}$) to the average utilization factor (U_{avg}).

$$\underbrace{\frac{\int_{t=\left(\omega_{i,j}-\theta_{i,j}/2\right)/360/f}^{\left(\omega_{i,j}+\theta_{i,j}/2\right)/360/f} \dot{m}_{i,j}\mathrm{d}t \bullet c_f}{m_{MCM,i} \bullet c_s}}_{U_{i,j}} = \underbrace{\frac{\dot{m}_{pump}/f \bullet c_f}{\sum_{i=1}^{13} m_{MCM,i} \bullet c_s}}_{U_{avg}} \tag{10}$$

where f and $m_{MCM,i}$ denote the frequency and the MCM mass at the ith AMR, respectively. The primary advantage of the identical utilization factor method is its significantly reduced computational complexity, as it avoids iterative AMR model calculations.

2. Identical outlet temperature method: The controller determines the solenoid valve opening period by minimizing the z-score values of AMR outlet temperatures. This process involves a two-step optimization approach [76]. Initially, a stochastic search using a genetic algorithm is employed to explore the solution space and prevent convergence to local optima. The genetic algorithm generates a predefined number of random vectors (population size), each of which is evaluated using individual AMR models for simulation and assessment. Penalty functions are applied if solenoid valve control limits are violated (Eq. (10)), and the vectors leading to non-converged simulations are rejected by assigning a significantly large objective function value. After each iteration of the genetic algorithm (generation), the population undergoes modifications such as mutation or crossover, resulting in a new set of vectors for evaluation in the subsequent generation. This process continues until the maximum number of generations is reached. The population size is set to 800, with a maximum of 1000 generations. A crossover probability of 0.85 and a mutation rate of 0.01 are selected. Once the genetic algorithm terminates, the best solution is selected as the initial guess for deterministic nonlinear optimization using the Levenberg–Marquardt method to refine the solution. The pretreatment using the genetic algorithm effectively avoids local minima and ensures solution convergence. The outlet temperature-based model predictive control is implemented periodically to update the valve setting and aid in control convergence.

$$\min F = \sum_{j=1}^{2}\left(\sum_{i=1}^{13}\left|z_{i,j}\right|\right) + \varphi\sum_{j=1}^{2}\left(\sum_{i=1}^{13}\left|h\left(\theta_{i,j}\right)\right|\right) \tag{11}$$

$$h\left(\theta_{i,j}\right) = \max\left[0, \left(\theta_{i,j} - \theta_{max}\right)\right] \tag{12}$$

where φ is a coefficient for the penalty term in the objective function, set to a large positive value. θ_{max} is the maximum allowable variation of the valve opening period (control limit). Note that both the genetic algorithm and nonlinear optimization utilize the same loss function (Eq. (12)). The final convergence is determined by the loss function of the nonlinear optimization, which allows for a certain tolerance in the error of the genetic algorithm. The stopping criterion for the genetic algorithm is defined by either reaching the threshold value of the loss function or the maximum number of iterations.

3. Results

In this section, the performance variations and control strategies implemented in the MCHP prototype are investigated. The dynamics of solenoid valve adjustments and their impact on system performance under different measurement feedback control methodologies are first experimentally analyzed. Subsequently, the effectiveness of various model predictive control strategies in enhancing heating capacity and COP across diverse operating conditions is numerically studied. Additionally, the implications of these results for advancing control strategies for parallel multi-bed MCHP systems in low-carbon building applications are discussed.

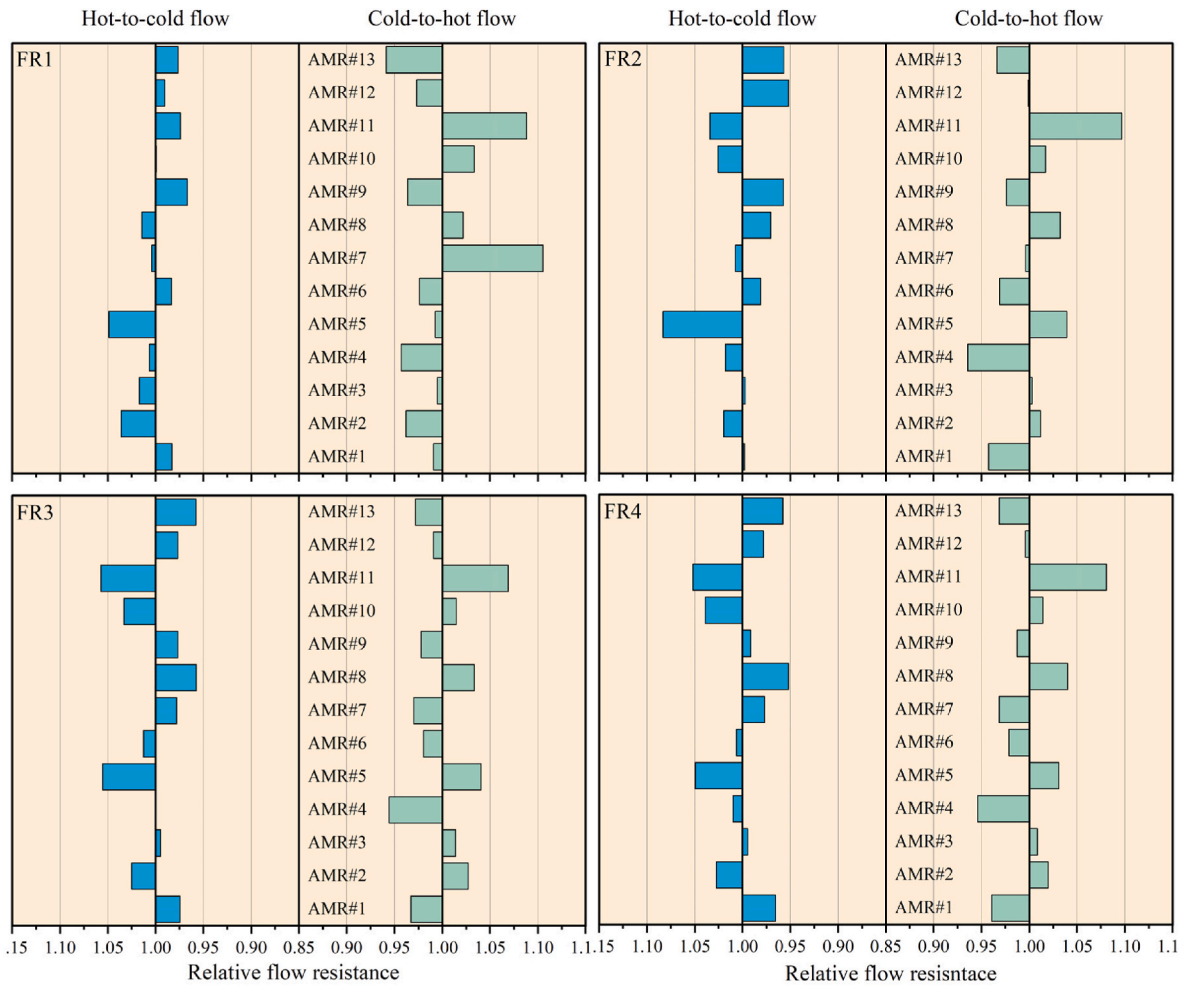

Fig. 6. Distribution of relative flow resistance among AMRs under four fluid flow rates: FR 1 (88.8–108.8 L/h), FR 2 (157.7–200.8 L/h), FR 3 (260.0–286.9 L/h), and FR 4 (332.4–362.8 L/h).

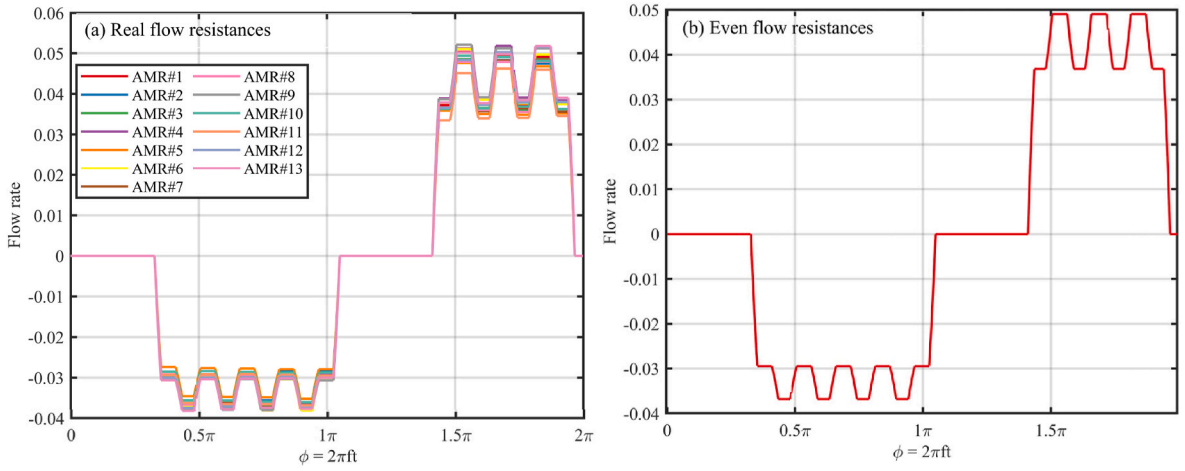

Fig. 7. Flow profiles for each AMR based on (a) real flow resistances and (b) even flow resistance.

3.1. *Fluid flow distribution*

The relative flow resistances for both the hot-to-cold and cold-to-hot directions, corresponding to four fluid flow rates—are depicted in Fig. 6. According to the definition of relative flow resistance in Eq. (5), deviations in flow resistance ranging from −5.5 % (in AMR#4, cold-to-hot direction) to +9.5 % (in AMR#11, cold-to-hot direction) are observed. Each solenoid valve has an opening phase angle that corresponds to the timing of fluid flow in its respective direction. As the magnets rotate, the current encoder phase angle falls within the opening phase angle range of certain solenoid valves. At this moment, these specific AMRs (3–4 AMRs in this study) share the pumped fluid flow. The degree of

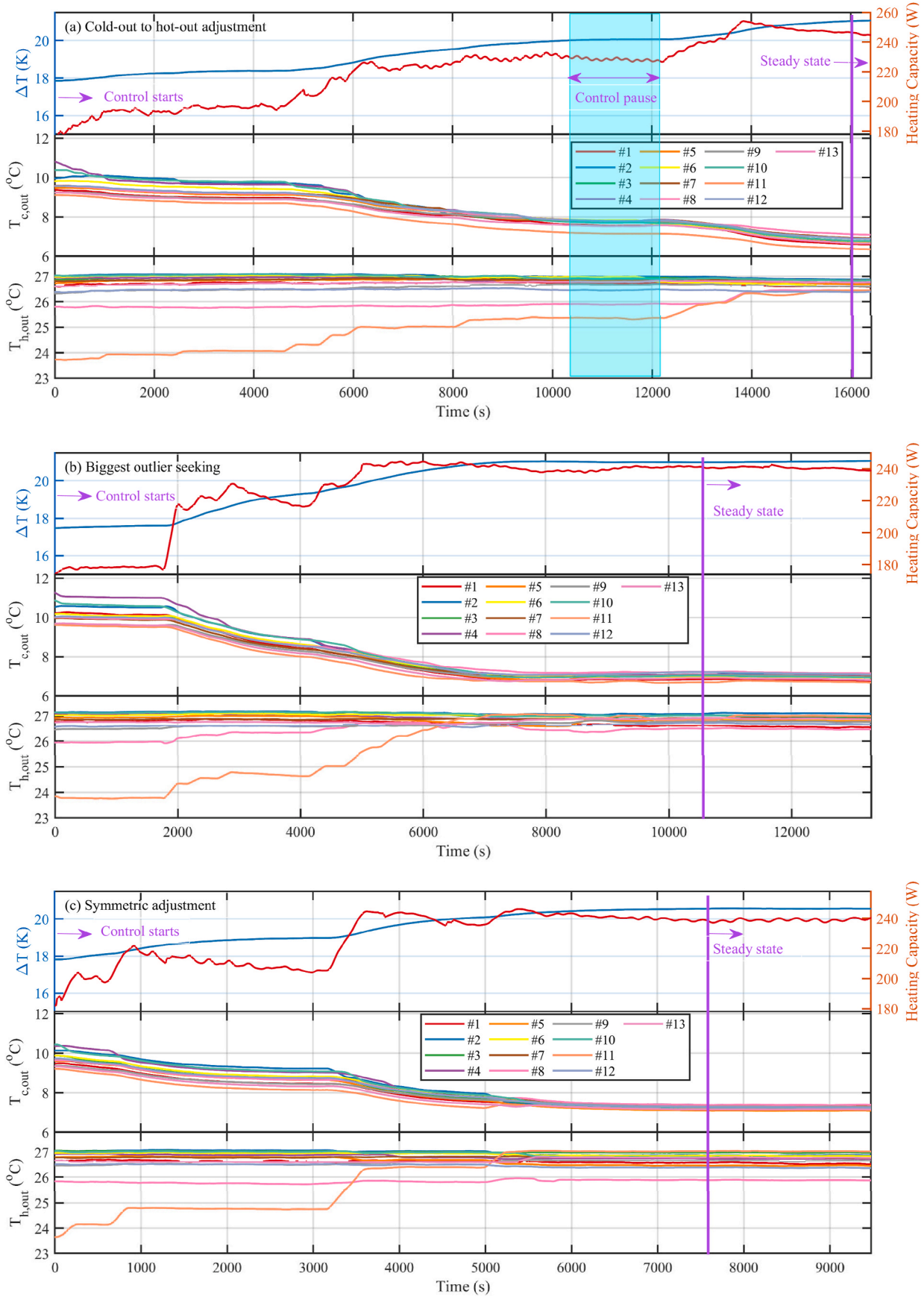

Fig. 8. Dynamic data illustrating the temperature span, heating capacity, as well as the cold-out and hot-out temperatures of all the AMRs for the prototype based on (a) cold-out to hot-out adjustment, (b) biggest outlier seeking, and (c) symmetric adjustment.

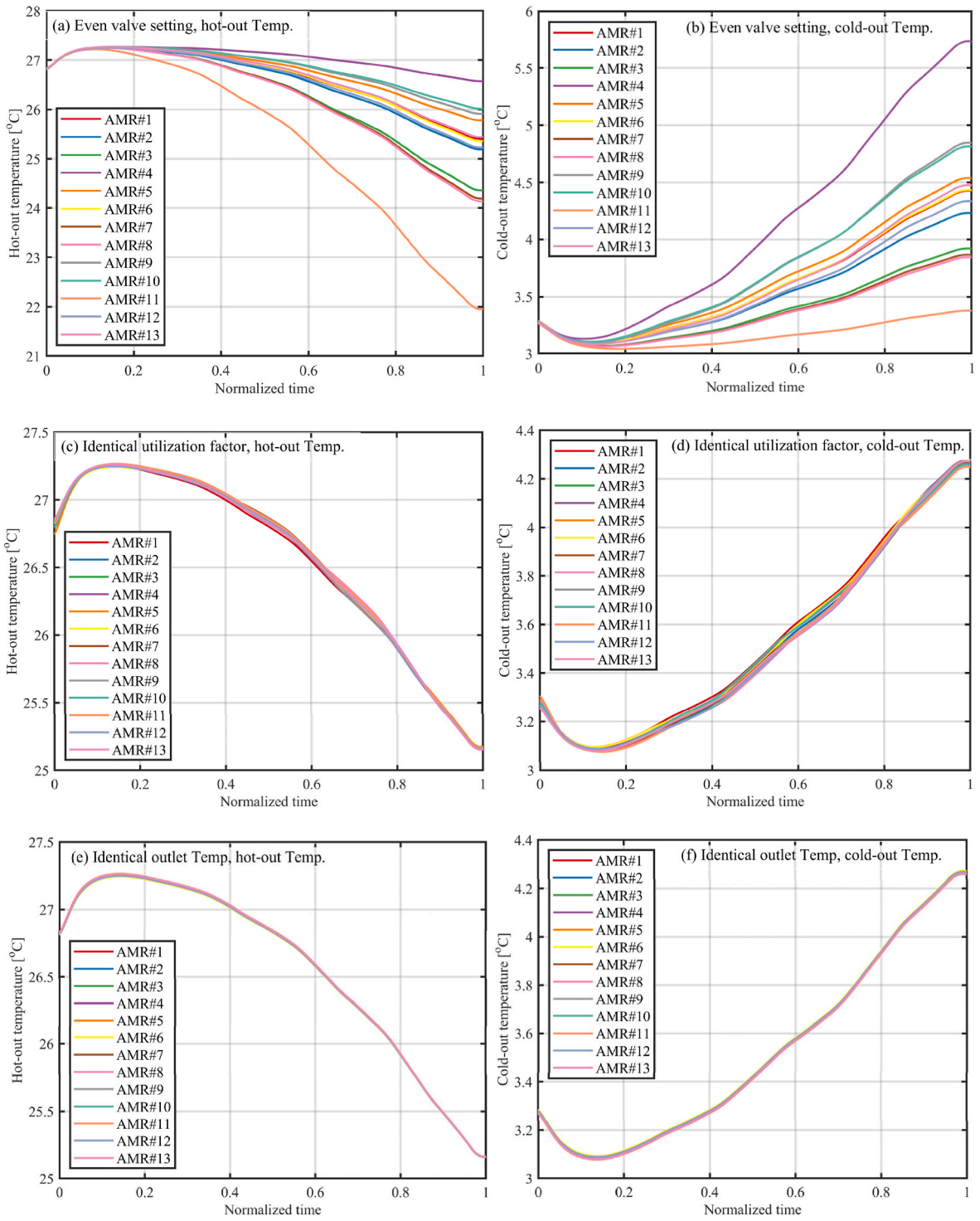

Fig. 9. Temperature profiles of AMR hot-out (a, c, e) and cold-out (b, d, f) under a selected operating condition identical to that discussed in Section 3.2. The profiles are analyzed based on (a–b) even valve setting, (c–d) identical utilization factor control, and (e–f) identical outlet temperature control. The normalized time represents the relative time over a blow period.

maldistribution among AMRs is directly influenced by the variation of fluid flow among neighboring 3–4 AMRs. For instance, AMR#11 within the AMR#10-AMR#13 group, displaying a relatively large standard deviation, is likely to encounter significant flow unbalance.

The flow profiles for the thirteen AMRs, both with and without accounting for flow resistance maldistribution, are illustrated in Fig. 7. The zigzag pattern on the plateau reflects the alternating distribution between 3 and 4 AMRs sharing the pumped flow. The areas bounded by the fluid profiles and the x-axis in the positive y-region and negative y-region represent the volume of pumped fluid for the specific AMR in the hot-to-cold direction and cold-to-hot direction, respectively. Variations in these enclosed areas in Fig. 7 highlight both intra- and inter-AMR flow unbalances.

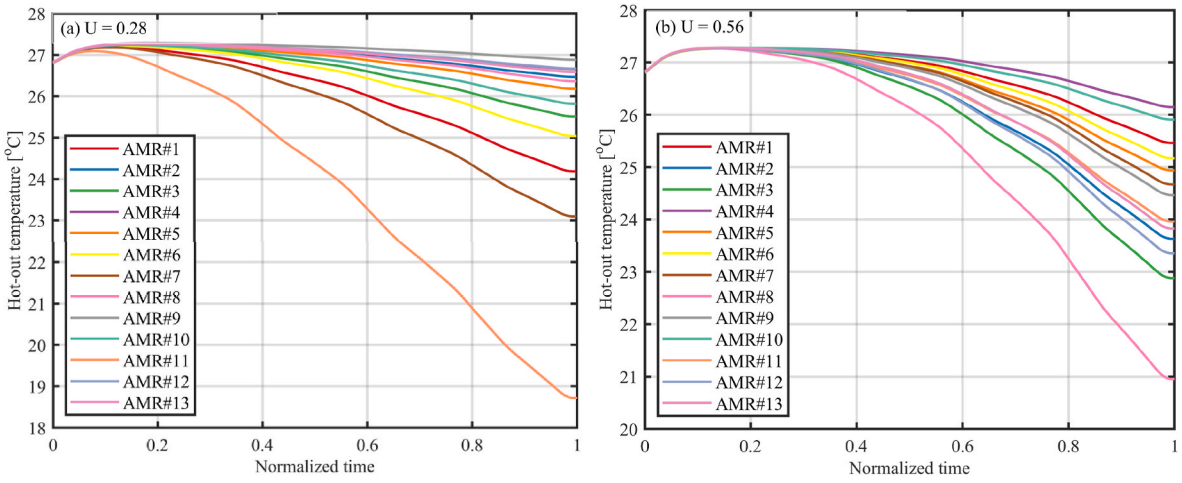

Fig. 10. Comparative analysis of AMR outlet temperatures under two utilization factors based on even valve setting.

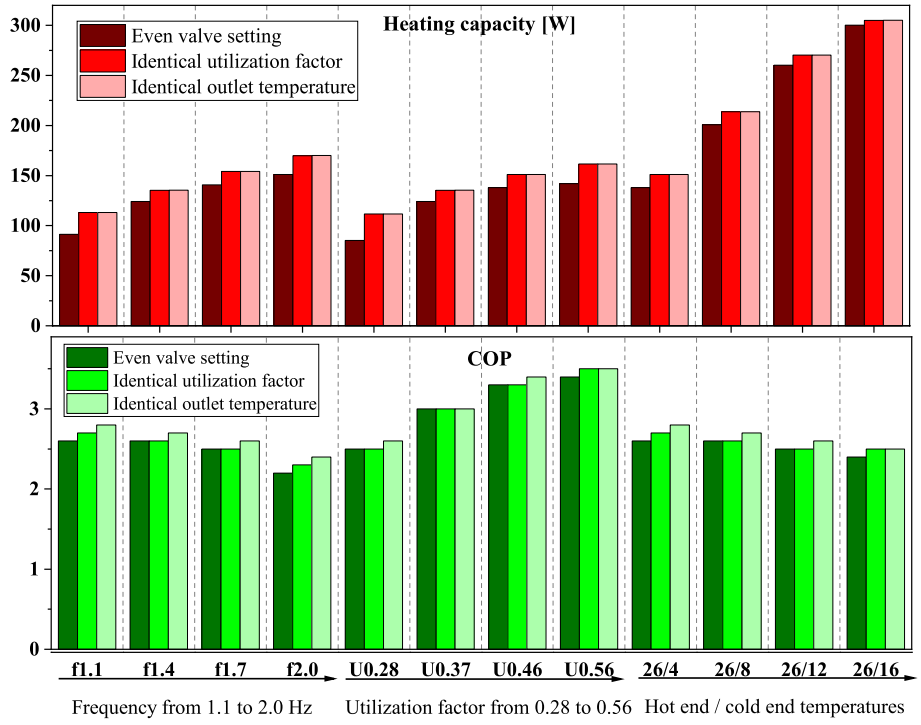

Fig. 11. Heating capacity and COP prediction under various operating conditions based on even valve setting, Identical utilization factor control, and identical outlet temperature control.

3.2. Controllability evaluation of measurement feedback control

The measurement feedback control strategies are activated in the prototype once a steady state is reached, using identical opening periods for the solenoid valves ($\theta_{1,j} = \theta_{2,j} = \cdots = \theta_{13,j}$). For brevity, a representative case study with significant outliers is presented in Fig. 8. The cold and hot reservoir temperatures are set at 26 °C and 4 °C, respectively, with an operating frequency of 1.4 Hz.

When the solenoid valves have identical opening periods, the outlet temperatures of individual AMRs can differ by several degrees. An AMR with higher flow resistance will have a lower fluid flow rate and colder cold-out temperatures, leading to a larger temperature span and reduced cooling capacity. As the MCM temperature drops, the AMR becomes more magnetic and is drawn towards the high-field regions of the rotating magnet. Meanwhile, the increased flow resistance in an AMR is usually due to lower porosity and a higher MCM fill level, which both require more magnetic work during operation. This combination results in increased torque required to rotate the magnet away from the cold regenerator, thereby prolonging the time which the colder AMRs spend within the magnetic field. This delay is because the motor cannot rotate as swiftly under the added load. Since the flow control is position-based, the colder AMRs receive more flow in the cold-to-hot direction, further cooling them. Consequently, these colder AMRs receive less fluid during hot-to-cold blows and more during cold-to-hot blows, exacerbating intra-AMR flow imbalances, and vice versa for warmer AMRs. This situation also intensifies the maldistribution between AMRs (inter-AMR flow unbalance). Furthermore, slight variations in the mass of MCM across different AMRs also contribute to the dispersion of outlet temperatures.

As illustrated in Fig. 8 (a) for the cold-out to hot-out adjustment

Table 1
Individual heating capacity for each AMR under various operating conditions with different frequencies (f), utilization factors (U), and cold end temperatures (T_c), while the hot end temperatures are maintained at 26 °C. $Q_{h,0}$, $Q_{h,idu}$, and $Q_{h,idt}$ denote the heating capacities based on even valve setting, identical utilization factor control, and identical outlet temperature control, respectively.

AMRs	f = 1.4 Hz, U = 0.28, T_c = 4 °C			f = 1.4 Hz, U = 0.49, T_c = 16 °C			f = 1.7 Hz, U = 0.37, T_c = 4 °C		
	$Q_{h,0}$	$Q_{h,idu}$	$Q_{h,idt}$	$Q_{h,0}$	$Q_{h,idu}$	$Q_{h,idt}$	$Q_{h,0}$	$Q_{h,idu}$	$Q_{h,idt}$
#1	−20.9	10.0	10.6	−109.2	22.9	23.9	−112.2	11.5	12.0
#2	11.5	10.6	10.4	95.6	23.9	23.5	78.4	12.1	11.9
#3	98.4	10.5	10.8	185.6	23.4	24.3	164.0	11.8	12.3
#4	−227.1	10.1	10.8	−301.3	23.0	24.4	−300.8	11.5	12.3
#5	−55.3	11.1	10.1	−44.3	25.0	22.7	−52.8	12.8	11.5
#6	−19.1	9.9	10.3	−63.5	22.7	23.2	−69.5	11.3	11.7
#7	114.9	10.6	10.7	53.3	23.6	24.0	44.3	12.0	12.1
#8	120.8	10.7	10.2	321.0	23.5	22.9	287.7	12.0	11.6
#9	−97.5	10.2	10.5	−35.0	22.9	23.6	−47.2	11.5	12.0
#10	−97.8	10.6	10.4	−170.2	24.0	23.5	−171.3	12.2	11.9
#11	325.5	10.7	10.2	218.0	24.7	22.9	204.6	12.7	11.6
#12	−0.6	10.0	10.0	103.1	22.5	22.6	84.1	11.3	11.4
#13	−28.8	10.2	10.5	47.3	22.8	23.6	31.4	11.5	12.0

Table 2
Performance prediction of MCHP under various control strategies, with the same operating conditions and flow resistance distribution as detailed in Section 3.2, while employing different MCMs in AMR#4 with ~25 % reduction in MCE. The properties of all MCMs were obtained through differential scanning calorimetry (DSC) under various applied magnetic fields and validated against data from direct measurements of adiabatic temperature change.

Parameters	Even valve setting	Identical utilizatoin factor	Identical outlet temperature
Frequency [Hz]	1.4	1.4	1.4
Utilization factor	0.34	0.34	0.34
Hot end temperature [°C]	26	26	26
Cold temperature [°C]	4	4	4
Heating capacity [W]	180.1	225.3	252.8
Cooling COP	1.62	1.81	1.90

strategy, the deviation of AMR#4 cold-out temperature gradually decreases with the adjustment of valve opening periods. Subsequently, AMR#11 becomes the primary outlier for cold-out temperatures. Adjusting the valve for AMR#11 leads to an overall decrease in cold-out temperatures for all AMRs, indicating improved cooling and heating capacities. Meanwhile, the deviation of AMR#11 hot-out temperature also decreases notably. This indicates that adjusting the solenoid valve in the hot-to-cold direction impacts not only the cold-out temperature but also the hot-out temperature. While the adjustment for AMR#11 reaches its limits at around 8200 s, adjustments for other AMRs commence, resulting in further performance improvement. The heater power, utilized to simulate cooling capacity during the test, is kept constant to prevent temperature oscillations during control. Consequently, the heating capacity increases from 178.8 W to 231.4 W (a 29.4 % increase), while the temperature span simultaneously increases from 17.9 K to 20.1 K for the solely cold-to-hot solenoid valve adjustment. To assess the controllability of solely hot-to-cold solenoid valve adjustment, there is a manual control pause (~1800 s) as marked in Fig. 8 (a). Besides AMR#11 reaching its limits, AMR#8 still exhibits a significant deviation in hot-out temperatures, prompting control for solenoid valves in the cold-to-hot direction. Following the phase of cold-to-hot solenoid valve adjustment, deviations in both cold-out and hot-out temperatures are within 1 K, leading to an additional 1 K (21.1 K) of temperature span and 13.4 W more in heating capacity (244.8 W, further 7.5 % increase). This underscores that decreasing valve opening periods in the cold-to-hot direction and/or increasing opening angles in the hot-to-cold direction for the AMRs colder than average can improve the heat pump performance.

Fig. 8 (b) shows the performance trend with the biggest outlier control strategy. AMR#4 emerges as the biggest outlier for cold-out temperatures, while AMR#11 is the biggest outlier for hot-out temperatures. In this case, both the z-score values of AMR#8 and AMR#11 exceed the threshold value, the controller concurrently adjusts these AMRs using solenoid valves in the cold-to-hot direction. Unlike the cold-out to hot-out adjustment strategy, it is observed that both the cold-out and hot-out temperatures of AMR#11 can be effectively controlled within the control limits. In this case study, adjusting the hot-out temperature rather than the cold-out temperature proves more suitable for AMR#11. While adjustments in the cold-to-hot or hot-to-cold direction affect both AMR hot-out and cold-out temperatures, the temperatures are predominantly influenced by the opening periods of solenoid valves in the respective directions. Consequently, the biggest outlier control strategy facilitates precise timing adjustments for each solenoid valve in the multi-bed scaled-up MCHP.

The symmetric adjustment control strategy aims to simplify the control process by utilizing half of the thermocouples (only cold-out temperatures) and reducing the control steps (simultaneously adjusting two conjugate solenoid valves). The performance results are shown in Fig. 8 (c). A faster steady-state is achieved in approximately 7600 s, with a temperature deviation of less than 0.5 K for cold-out temperatures. Since the controller identifies outliers based solely on cold-out temperatures, as defined by the symmetric adjustment in Section 2.2, the hot-out temperature of AMR#8 is not flagged as an outlier and is therefore not effectively controlled. This highlights an asymmetric distribution in the deviations of AMR cold-out and hot-out temperatures, necessitating tailored adjustments for specific AMRs at either cold-out or hot-out temperatures. In this scenario, the temperature span of the MCHP using the symmetric adjustment control strategy is 20.4 K, less than 21.0 K achieved with other control strategies.

3.3. Simulation assessment of model predictive control

The measurement feedback control method discussed in Section 3.2 exhibits prolonged control convergence times, owing to adjusting valve settings either one at a time or multiple valves only after surpassing the thresholds for preventing control overshooting. Given the necessity to adjust 26 solenoid valves and to allow for waiting periods for steady state between adjustments to prevent control chaos, the control convergence time ranges between 7600 and 14200 s in Section 3.2. To improve this, model predictive control provides an estimate with multiple valve settings, refined by iteratively updating model parameters through real-time measurements. The accuracy of these valve setting estimates directly affects the control convergence time. Fig. 9 illustrates variations in cold-out and hot-out temperatures using even valve opening, the identical utilization factor method, and the identical outlet

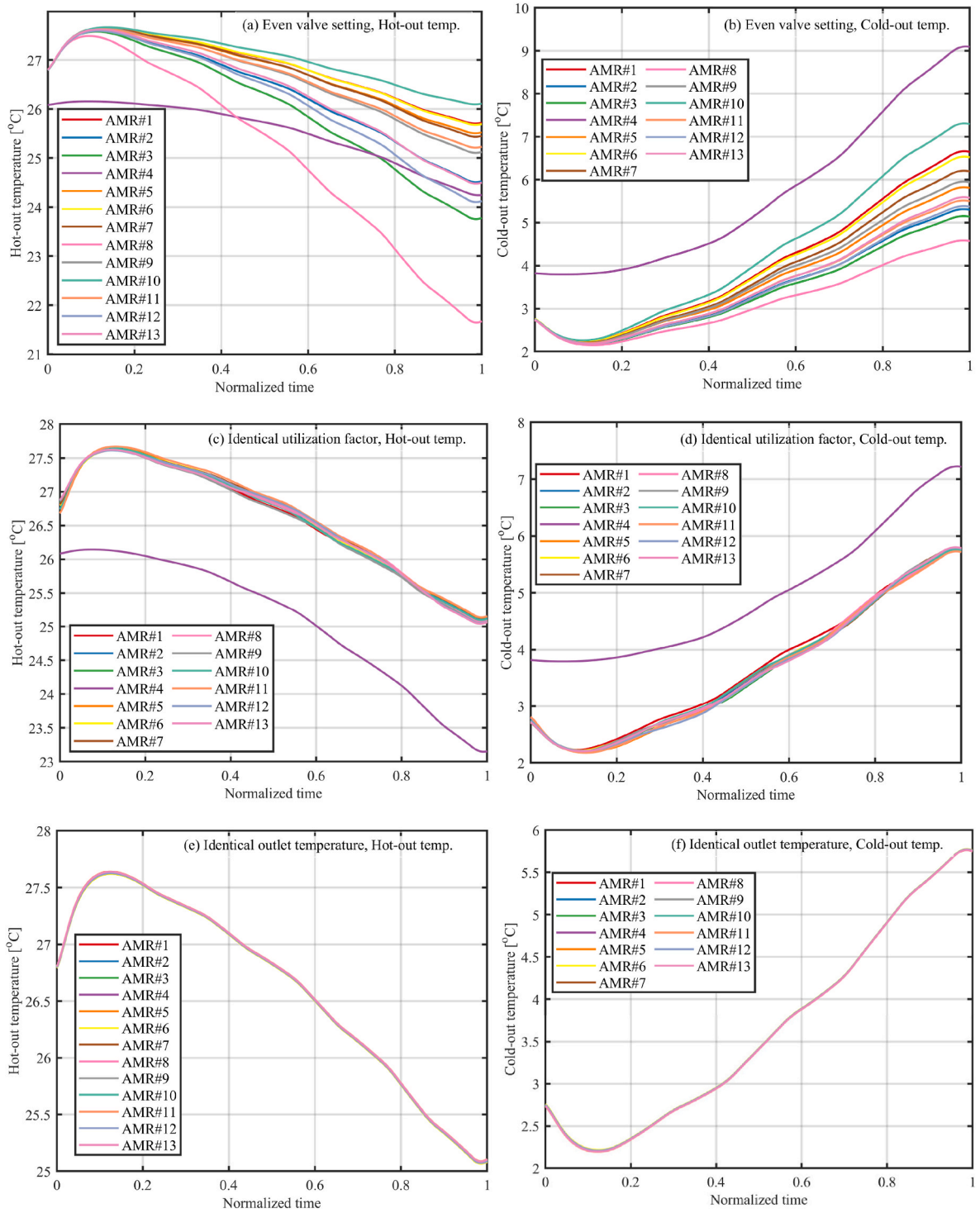

Fig. 12. Temperature profiles of AMR hot-out (a, c, e) and cold-out (b, d, f) under a real flow resistance distribution, with different MCMs are applied in AMR#4. The profiles are analyzed based on (a–b) even valve setting, (c–d) identical utilization factor control, and (e–f) identical outlet temperature control.

temperature method. The inconsistencies among AMRs are employed in the flow resistance distribution and MCM charge masses detailed in Section 3.1. A temperature variation range of 2.3 K for cold-out temperatures and 4.6 K for hot-out temperatures is observed in simulations with even valve settings. These estimates align reasonably well with the experimental data presented in Section 3.2. Notably, the model accurately predicts the largest outliers, AMR#11 and AMR#8 for hot-out temperatures and AMR#4 for cold-out temperatures, though some disparities between model predictions and measurements exist in outlier rankings. This discrepancy may stem from not accounting for the impact of magnetic force on rotation speed in the model. When employing the identical utilization factor method, temperature variation ranges for both cold-out and hot-out temperatures narrow to within 0.03 K, highlighting the efficacy in temperature regulation. Implementing the solenoid valve settings with the identical outlet temperature method further minimizes temperature variations. This underscores the precision in valve setting prediction, albeit at the cost of increased computational overhead.

Given the complex interplay between AMR arrangement, flow resistance, and MCM, the ranking of outliers of AMR outlet temperatures varies across different operating conditions, as depicted in Fig. 10. For instance, the hot-out temperature profiles under two different working conditions reveal distinct outlier rankings. At a utilization factor of 0.28, the top-three outliers are AMR#11, AMR#7, and AMR#1, while at a utilization factor of 0.56, they are AMR#8, AMR#3, and AMR#12. This highlights the need for dynamic control to accommodate the flexible operation of MCHP, even though flow resistance can be measured beforehand.

The performance variations in response to solenoid valve settings based on the identical utilization factor and identical outlet temperature methods are illustrated in Fig. 11. Compared to even valve settings, the identical utilization factor method across selected operating conditions shows improvements of 1.6 %–30.9 % in heating capacity and 1.2 %–10.7 % in COP. Additionally, when the computationally intensive identical outlet temperature method is applied, further improvements of ~0.1 % in heating capacity and ~3.5 % in COP are observed. This implies that while the identical outlet temperature method offers moderate improvements in COP, its benefit in enhancing heating capacity is marginal. There is no clear trend of performance improvements as a function of utilization factor and frequency. In contrast, the heating capacity improvement increases from 1.6 % to 9.6 % as the temperature span increases from 10 K to 22 K, highlighting the greater necessity for applying control strategies in MCHP systems with higher temperature spans. Another observation from Fig. 11 is that the model predictive improvement in heating capacity is less pronounced compared to the experimental results. This disparity arises from overestimating MCHP performance under even valve settings due to neglecting the influence of magnetic forces on rotation speed, which exacerbates the uneven distribution of heating capacity across the AMRs.

The mechanism of performance improvement through solenoid valve opening time control can be visualized by comparing individual AMR heating capacities under even valve setting, identical utilization factor control, and identical outlet temperature control. Simulating the individual AMR heating capacities as illustrated in Table 1, a significant disparity in heating capacities among the 13 AMRs is observed. This disparity primarily arises from intra-AMR flow unbalance, leading to substantial exergy destruction. Upon applying identical utilization factor control, the variations in individual AMR heating capacities are reduced to within 2 W. Furthermore, adopting identical outlet temperature control results in nearly uniform distribution of heating capacities across the AMRs. The slight remaining variations in individual AMR heating capacity are attributed to differences in porosities between the AMRs.

The primary objective of developing model predictive control is to provide multiple valve settings in a single estimation that closely approximate the final settings. Table A in Appendix A displays the opening periods for all solenoid valves based a single model prediction, derived from both the identical utilization factor method and the identical outlet temperature method, along with the valve final setting under measurement feedback control. The differences in valve setting predictions between the two model methods are minimal (<0.3°), indicating that utilizing the identical utilization factor control—with significantly lower computational expenses—can serve as a substitute for the identical outlet temperature control, given that only the effects of uneven flow resistance and MCM mass between AMRs are considered. When comparing the valve settings predicted by the model with those obtained from measurement feedback control, the model predictive valve settings for significant outliers (e.g., AMR#11 in cold-to-hot direction and AMR#4 in hot-to-cold direction) approach the final setting from the measurement feedback control. However, some valve predictive settings are excessive, particularly for smaller outliers, although these variations are assumed to have a minor impact on the system performance. Here the effective step length (n) is defined as the progressive step length from the initial valve setting towards the final setting.

$$n(\theta_{\text{estimate}}) = \left|\theta_{\text{final}} - \theta_{\text{inital}}\right| - \left|\theta_{\text{estimate}} - \theta_{\text{initial}}\right| \tag{13}$$

The total step length is defined as the cumulative change in the opening angles, measured in degrees, for all the solenoid valves from their initial to final states ($\Delta\theta_{\text{cold}} + \Delta\theta_{\text{hot}}$). For the case studies presented in Table A, total step lengths required for measurement feedback control are 35 at a frequency of 1.4 Hz and 39 at a frequency of 1.1 Hz. In these case studies, as discussed in Section 3.2, the step length of measurement-feedback control is only 1 or 2 (for the biggest outlier and outliers exceeding the threshold) per iteration. In contrast, the cumulative effective step lengths using model predictive identical utilization factor control are 14.4 (8.2 + 6.2) at a frequency of 1.4 Hz and 15.4 (8.6 + 6.8) at a frequency of 1.1 Hz, representing approximately a seven-fold increase in control convergence speed compared to the measurement feedback control strategy. This indicates that the model predictive method provides an efficient means for rapidly tuning parallel multi-bed MCHP systems. With future digital twin implementation, the model accuracy is expected to improve through periodic model parameter updates, further reducing the required iteration steps (estimated from $(\Delta\theta_{\text{cold}} + \Delta\theta_{\text{hot}})/(\sum n_{\text{cold}} + \sum n_{\text{hot}})$).

4. Discussion

Achieving suitable fluid flow across parallel AMRs is essential for scaling up MCHP in low-carbon building systems. This study explores the feasibility of adjusting individual fluid flow using a solenoid valving system, resulting in heating capacity improvements of 36.9 % in experiments and 1.2 %–10.7 % in modeling. A significant drawback observed is the prolonged control convergence time with current control strategies. Model predictive control offers a solution to expedite control convergence by providing an initial valve setting estimation for all valves in a single step. While the predictive valve setting of current model achieves positive results for major outliers, it tends to overshoot for minor ones. The limitations of this study include the absence of model predictive magnet motion integrated with the AMR model for a more accurate valve setting estimation. The absence of torque analysis and precise prediction of magnet motion profiles can cause deviations in model predictive control. Additionally, achieving precise model predictions often requires real-time measurement data training, presenting a demand to fully implement digital twin control. To improve the effectiveness of these control strategies, future steps involve establishing a local supervisory control and data acquisition system capable of storing extensive operational data and periodically validating the model. However, model-based approaches may oversimplify uncertainties related to data collection, such as measurement errors and state estimations. Moreover, MCHP performance can deteriorate over time due to component wear or changes in boundary conditions. Integrating model predictive control frameworks with machine learning algorithms can help identify potential system failures, such as component aging, in advance.

Another limitation of this study is the absence of a techno-economic analysis, which is necessary to evaluate the trade-off between the additional costs of implementing various control strategies and the potential operating cost savings achieved through improved efficiency. For measurement-feedback controls, the additional cost primarily involves thermocouples for monitoring AMR outlet temperatures, which is expected to be significantly lower than the operating cost savings from reduced energy consumption. Future research will focus on optimizing component costs to enable a more accurate techno-economic analysis.

The identical utilization factor control strategy assumes a uniform MCE across the MCM in each AMR, making it ideal for systems that use pure second-order gadolinium (Gd) as the MCM. In contrast, first-order MCMs represent another emerging direction. However, their effective MCE is limited to a narrow temperature range, necessitating the

development of multi-layer AMRs in recent devices [77–79]. To achieve a practical temperature span (<20K) for MCHP, various MCM compositions with distinct transition temperatures are arranged sequentially along the fluid flow direction to optimize local MCE. For the commercialized La(Fe,Mn,Si)$_{13}$H$_y$ MCM, a Curie temperature variation of ~ ±2 K and an adiabatic temperature change deviation of ~25 % can be expected within the same batch of existing MCMs, leading to the risk of uneven MCE between AMRs. Scaling up MCHP with layered La(Fe,Mn,Si)$_{13}$H$_y$ introduces challenges associated with uneven MCE between AMRs, which can complicate hydraulic control. This complexity may render the identical utilization factor control strategy ineffective.

Table 2 compares the performance under even valve settings, identical utilization factor control, and identical outlet temperature control when a different batch of La(Fe,Mn,Si)$_{13}$H$_y$ with approximately a 25 % reduction in adiabatic temperature change is used in AMR#4. Under the real flow resistance distribution among AMRs as above and varying MCMs in AMR#4, identical utilization factor control improves heating capacity from 180.1 W to 225.3 W and COP from 1.62 to 1.81. Further improvements to heating capacity (252.8 W) and COP (1.90) are achieved with identical outlet temperature control. While Fig. 12 illustrates how identical utilization factor control addresses diverse flow resistances among AMRs more effectively than MCE variation, precise model predictive control based on identical outlet temperature becomes improvement for complex MCHP operations with varying MCM properties. However, considering Curie temperature shifting in layered AMRs, merely aligning outlet temperatures may result in some AMRs operating beyond their transition temperatures. Therefore, control strategies utilizing digitalization and optimization programs are vital for balancing operating MCE maximization due to Curie temperature shift, and exergy destruction minimization due to fluid mixing with different temperatures in the manifold.

By comparing Fig. 11 and Table 2, the impact of MCM properties across multiple beds on the overall system efficiency can be assessed. When operating with cold and hot reservoir temperatures set at 4 °C and 26 °C, respectively, and a frequency of 1.4 Hz, the transition from Gd to layered La(Fe,Mn,Si)$_{13}$H$_y$ as the MCM increases the heating capacity from 152.4 W to 258.8 W, while the COP decreases from 2.68 to 1.90. This improvement in heating capacity highlights the need to optimize the layering of La(Fe,Mn,Si)$_{13}$H$_y$ to enhance overall efficiency.

5. Conclusions

This study investigates the challenges and opportunities of scaling up magnetocaloric heat pump performance in low-carbon building systems. Factors like uneven flow resistance, porosity, and magnetocaloric effect negatively impact the heat pump efficiency in parallel multi-bed configurations. Two primary control strategies, measurement feedback control and model predictive control, were explored to optimize fluid flow through the regenerators. Through experimental and numerical studies, key findings include.

1. **Measurement Feedback Control** enhances heating capacity by 36.9 % but requires a lengthy control convergence time of at least 7600 s.
2. **Biggest Outlier Seeking Control** outperforms the cold-out hot-out adjustment and symmetric adjustment strategies due to its ability to account for complex correlations between valve settings and regenerator temperatures.
3. **Model Predictive Control** achieves positive results for major outliers, demonstrating the potential for faster control convergence, while addressing overshooting for minor outliers requires further refinement. The control convergence speed is estimated to be seven times faster compared to the measurement feedback control strategy.
4. **Utilization Factor-Based Model Predictive Control** increases heating capacity by 1.6 %–30.9 % and COP by 1.2 %–10.7 % in scenarios characterized by uneven flow resistance and porosity, all while minimizing computational costs. However, its effectiveness relies on the assumption of uniform magnetocaloric effects across regenerators.
5. **Outlet Temperature-Based Model Predictive Control** further improves COP by ~3.5 %, accommodating uneven magnetocaloric effects but requiring increased computational resources with stochastic search.

Despite advancements in magnetocaloric heat pumps, challenges remain, particularly in adapting control strategies to multi-layer regenerators with varying Curie temperatures and magnetocaloric effects. Future work could explore advanced control methods, such as digital twin integration, coupled with optimization algorithms such as machine learning, to effectively manage flexible operating conditions in renewable energy building systems.

CRediT authorship contribution statement

Jierong Liang: Writing – original draft, Visualization, Validation, Resources, Methodology, Investigation, Formal analysis, Conceptualization. **Marvin Masche:** Visualization, Validation, Resources, Investigation, Formal analysis, Data curation. **Kun Wang:** Writing – review & editing, Visualization, Validation, Resources, Formal analysis. **Tim Sittig:** Supervision, Resources, Project administration. **Dimitri Benke:** Writing – review & editing, Visualization, Supervision, Resources, Methodology. **Maximilian Fries:** Supervision, Project administration, Funding acquisition. **Kurt Engelbrecht:** Writing – review & editing, Validation, Supervision, Resources, Methodology, Formal analysis, Conceptualization. **Christian R.H. Bahl:** Writing – review & editing, Validation, Supervision, Resources, Project administration, Funding acquisition, Formal analysis.

Declaration of competing interest

The authors declare that they have no known competing financial interests or personal relationships that could have appeared to influence the work reported in this paper.

Data availability

Data will be made available on request.

Acknowledgments

This work was financed by the MicroChMag project, which received funding from the European Union's Horizon research and innovation program under the Marie Sklodowska-Curie grant agreement No. 101066427. The authors wish to acknowledge the RES4Build project, which received funding from the European Union's Horizon 2020 research and innovation program under grant agreement No. 814865.

Appendix A. Supplementary data

Supplementary data to this article can be found online at https://doi.org/10.1016/j.energy.2024.133245.

References

[1] European commission. Heat pumps n.d.
[2] European Commission. REPowerEU: Affordable, secure and sustainable energy for Europe n.d.
[3] McLinden MO, Seeton CJ, Pearson A. New refrigerants and system configurations for vapor-compression refrigeration. Science (80-) 2020;370:791–6. https://doi.org/10.1126/science.abe3692.
[4] Gao P, Wang LW, Zhu FQ. A novel hybrid solid sorption-compression refrigeration technology for refrigerated transportation and storage. Int J Refrig 2021;122:1–10. https://doi.org/10.1016/j.ijrefrig.2020.10.041.

[5] Ismail M, Yebiyo M, Chaer I. A review of recent advances in emerging alternative heating and cooling technologies. Energies 2021;14:502. https://doi.org/10.3390/en14020502.

[6] Qian S, Nasuta D, Rhoads A, Wang Y, Geng Y, Hwang Y, et al. Not-in-kind cooling technologies: a quantitative comparison of refrigerants and system performance. Int J Refrig 2016;62:177–92. https://doi.org/10.1016/j.ijrefrig.2015.10.019.

[7] Steven Brown J, Domanski PA. Review of alternative cooling technologies. Appl Therm Eng 2014;64:252–62. https://doi.org/10.1016/j.applthermaleng.2013.12.014.

[8] Czernuszewicz A, Kaleta J, Lewandowski D. Multicaloric effect: toward a breakthrough in cooling technology. Energy Convers Manag 2018;178:335–42. https://doi.org/10.1016/j.enconman.2018.10.025.

[9] Moya X, Mathur ND. Caloric materials for cooling and heating. Science (80-) 2020;370:797–803. https://doi.org/10.1126/science.abb0973.

[10] Aprea C, Greco A, Maiorino A, Masselli C. The employment of caloric-effect materials for solid-state heat pumping. Int J Refrig 2020;109:1–11. https://doi.org/10.1016/j.ijrefrig.2019.09.011.

[11] Sari O, Balli M. From conventional to magnetic refrigerator technology. Int J Refrig 2014;37:8–15. https://doi.org/10.1016/j.ijrefrig.2013.09.027.

[12] Kitanovski A, Plaznik U, Tomc U, Poredoš A. Present and future caloric refrigeration and heat-pump technologies. Int J Refrig 2015;57:288–98. https://doi.org/10.1016/j.ijrefrig.2015.06.008.

[13] Ahčin Ž, Dall'Olio S, Žerovnik A, Už Baškovič, Porenta L, Kabirifar P, et al. High-performance cooling and heat pumping based on fatigue-resistant elastocaloric effect in compression. Joule 2022;6:2338–57. https://doi.org/10.1016/j.joule.2022.08.011.

[14] Qian S, Catalini D, Muehlbauer J, Liu B, Mevada H, Hou H, et al. High-performance multimode elastocaloric cooling system. Science 2023;380(80):722–7. https://doi.org/10.1126/science.adg7043.

[15] Tušek J, Engelbrecht K, Eriksen D, Dall'Olio S, Tušek J, Pryds N. A regenerative elastocaloric heat pump. Nat Energy 2016;1:16134. https://doi.org/10.1038/nenergy.2016.134.

[16] Aprea C, Greco A, Maiorino A, Masselli C. The use of barocaloric effect for energy saving in a domestic refrigerator with ethylene-glycol based nanofluids: a numerical analysis and a comparison with a vapor compression cooler. Energy 2020;190:116404. https://doi.org/10.1016/j.energy.2019.116404.

[17] Aprea C, Greco A, Maiorino A, Masselli C. Enhancing the heat transfer in an active barocaloric cooling system using ethylene-glycol based nanofluids as secondary medium. Energies 2019;12. https://doi.org/10.3390/en12152902.

[18] Aznar A, Lloveras P, Romanini M, Barrio M, Tamarit JL, Cazorla C, et al. Giant barocaloric effects over a wide temperature range in superionic conductor AgI. Nat Commun 2017;8. https://doi.org/10.1038/s41467-017-01898-2.

[19] Shi J, Han D, Li Z, Yang L, Lu SG, Zhong Z, et al. Electrocaloric cooling materials and devices for zero-global-warming-potential, high-efficiency refrigeration. Joule 2019;3:1200–25. https://doi.org/10.1016/j.joule.2019.03.021.

[20] Ma R, Zhang Z, Tong K, Huber D, Kornbluh R, Ju YS, et al. Highly efficient electrocaloric cooling with electrostatic actuation. Science (80-) 2017;357:1130–4. https://doi.org/10.1126/science.aan5980.

[21] Wang Y, Zhang Z, Usui T, Benedict M, Hirose S, Lee J, et al. A high-performance solid-state electrocaloric cooling system. Science 2020;370(80):129–33. https://doi.org/10.1126/science.aba2648.

[22] Klinar K, Kitanovski A. Thermal control elements for caloric energy conversion. Renew Sustain Energy Rev 2020;118:109571. https://doi.org/10.1016/j.rser.2019.109571.

[23] Hou H, Qian S, Takeuchi I. Materials, physics and systems for multicaloric cooling. Nat Rev Mater 2022;7:633–52. https://doi.org/10.1038/s41578-022-00428-x.

[24] Zhang Y, Wu J, He J, Wang K, Yu G. Solutions to obstacles in the commercialization of room-temperature magnetic refrigeration. Renew Sustain Energy Rev 2021;143:110933. https://doi.org/10.1016/j.rser.2021.110933.

[25] Torelló A, Defay E. Electrocaloric coolers: a review. Adv Electron Mater 2022;8. https://doi.org/10.1002/aelm.202101031.

[26] Engelbrecht K. Future prospects for elastocaloric devices. JPhys Energy 2019;1:021001. https://doi.org/10.1088/2515-7655/ab1573.

[27] RES4BUILD. Renewables for clean energy buildings in a future power system n.d.

[28] Mohamad Z, Fardoun F, Meftah F. A review on energy piles design, evaluation, and optimization. J Clean Prod 2021;292:125802. https://doi.org/10.1016/j.jclepro.2021.125802.

[29] Shen T, Xie H, Gavurová B, Sangeetha M, Karthikeyan C, T RP, et al. Experimental analysis of photovoltaic thermal system assisted with nanofluids for efficient electrical performance and hydrogen production through electrolysis. Int J Hydrogen Energy 2023;48:21029–37. https://doi.org/10.1016/J.IJHYDENE.2022.12.079.

[30] Kitanovski A. Energy applications of magnetocaloric materials. Adv Energy Mater 2020;1903741:1903741. https://doi.org/10.1002/aenm.201903741.

[31] Kitanovski A, Tušek J, Tomc U, Plaznik U, Ožbolt M, Poredoš A. Magnetocaloric energy conversion: from theory to applications. https://doi.org/10.1007/978-3-319-08741-2; 2015.

[32] Kitanovski A, Egolf PW. Thermodynamics of magnetic refrigeration. Int J Refrig 2006;29:3–21. https://doi.org/10.1016/j.ijrefrig.2005.04.007.

[33] Kamran MS, Ahmad HO, Wang HS. Review on the developments of active magnetic regenerator refrigerators – evaluated by performance. Renew Sustain Energy Rev 2020;133:110247. https://doi.org/10.1016/j.rser.2020.110247.

[34] Yu B, Liu M, Egolf PW, Kitanovski A. A review of magnetic refrigerator and heat pump prototypes built before the year 2010. Int J Refrig 2010;33:1029–60. https://doi.org/10.1016/j.ijrefrig.2010.04.002.

[35] Greco A, Aprea C, Maiorino A, Masselli C. A review of the state of the art of solid-state caloric cooling processes at room-temperature before 2019. Int J Refrig 2019;106:66–88. https://doi.org/10.1016/j.ijrefrig.2019.06.034.

[36] Romero Gómez J, Ferreiro Garcia R, Carbia Carril J, Romero Gómez M. A review of room temperature linear reciprocating magnetic refrigerators. Renew Sustain Energy Rev 2013;21:1–12. https://doi.org/10.1016/j.rser.2012.12.018.

[37] Tura A, Rowe A. Permanent magnet magnetic refrigerator design and experimental characterization. Int J Refrig 2011;34:628–39. https://doi.org/10.1016/j.ijrefrig.2010.12.009.

[38] Okamura T, Yamada K, Hirano N, Nagaya S. Performance of a room-temperature rotary magnetic refrigerator. Int J Refrig 2006;29:1327–31. https://doi.org/10.1016/j.ijrefrig.2006.07.020.

[39] Masche M, Liang J, Engelbrecht K, Bahl CRH. Performance assessment of a rotary active magnetic regenerator prototype using gadolinium. Appl Therm Eng 2022;204:117947. https://doi.org/10.1016/j.applthermaleng.2021.117947.

[40] Zimm C, Boeder A, Chell J, Sternberg A, Fujita A, Fujieda S, et al. Design and performance of a permanent-magnet rotary refrigerator. Int J Refrig 2006;29:1302–6. https://doi.org/10.1016/j.ijrefrig.2006.07.014.

[41] Lee H, Troch S, Hwang Y, Radermacher R. LCCP evaluation on various vapor compression cycle options and low GWP refrigerants. Int J Refrig 2016;70:128–37. https://doi.org/10.1016/j.ijrefrig.2016.07.003.

[42] Meggers F, Ritter V, Goffin P, Baetschmann M, Leibundgut H. Low exergy building systems implementation. Energy 2012;41:48–55. https://doi.org/10.1016/j.energy.2011.07.031.

[43] Zajacs A, Bogdanovics R, Borodinecs A. Analysis of low temperature lift heat pump application in a district heating system for flue gas condenser efficiency improvement. Sustain Cities Soc 2020;57. https://doi.org/10.1016/j.scs.2020.102130.

[44] Li Z, Shen J, Li K, Gao X, Guo X, Dai W. Assessment of three different gadolinium-based regenerators in a rotary-type magnetic refrigerator. Appl Therm Eng 2019;153:159–67. https://doi.org/10.1016/j.applthermaleng.2019.02.100.

[45] Velázquez D, Estepa C, Palacios E, Burriel R. A comprehensive study of a versatile magnetic refrigeration demonstrator. Int J Refrig 2016;63:14–24. https://doi.org/10.1016/j.ijrefrig.2015.10.006.

[46] Teyber R, Trevizoli PV, Christiaanse TV, Govindappa P, Niknia I, Rowe A. Performance evaluation of two-layer active magnetic regenerators with second-order magnetocaloric materials. Appl Therm Eng 2016;106:405–14. https://doi.org/10.1016/j.applthermaleng.2016.06.029.

[47] Eriksen D, Engelbrecht K, Haffenden Bahl CR, Bjørk R. Exploring the efficiency potential for an active magnetic regenerator. Sci Technol Built Environ 2016;22:527–33. https://doi.org/10.1080/23744731.2016.1173495.

[48] Jacobs S, Auringer J, Boeder A, Chell J, Komorowski L, Leonard J, et al. The performance of a large-scale rotary magnetic refrigerator. Int J Refrig 2014;37:84–91. https://doi.org/10.1016/j.ijrefrig.2013.09.025.

[49] Aprea C, Cardillo G, Greco A, Maiorino A, Masselli C. A rotary permanent magnet magnetic refrigerator based on AMR cycle. Appl Therm Eng 2016;101:699–703. https://doi.org/10.1016/j.applthermaleng.2016.01.097.

[50] Eriksen D, Engelbrecht K, Bahl CRH, Bjørk R, Nielsen KK. Effects of flow balancing on active magnetic regenerator performance. Appl Therm Eng 2016;103:1–8. https://doi.org/10.1016/j.applthermaleng.2016.03.001.

[51] Fortkamp FP, Lang GB, Lozano JA, Barbosa JR. Numerical analysis of the influence of magnetic field waveforms on the performance of active magnetic regenerators. J Brazilian Soc Mech Sci Eng 2020;42:378. https://doi.org/10.1007/s40430-020-02453-9.

[52] Bjørk R, Engelbrecht K. The influence of the magnetic field on the performance of an active magnetic regenerator (AMR). Int J Refrig 2011;34:192–203. https://doi.org/10.1016/j.ijrefrig.2010.07.004.

[53] Masche M, Liang J, Engelbrecht K, Bahl CRH. Efficient modulation of the magnetocaloric refrigerator capacity. Int J Refrig 2023;145:59–67. https://doi.org/10.1016/j.ijrefrig.2022.10.005.

[54] Griffith L, Czernuszewicz A, Slaughter J, Pecharsky V. Active magnetic regenerative cooling with smaller magnets. Int J Refrig 2021;125:44–51. https://doi.org/10.1016/j.ijrefrig.2021.01.018.

[55] Li Z, Li K, Guo X, Gao X, Dai W, Gong M, et al. Influence of timing between magnetic field and fluid flow in a rotary magnetic refrigerator. Appl Therm Eng 2021;187:116477. https://doi.org/10.1016/j.applthermaleng.2020.116477.

[56] Fortkamp FP, Eriksen D, Engelbrecht K, Bahl CRH, Lozano JA, Barbosa JR. Experimental investigation of different fluid flow profiles in a rotary multi-bed active magnetic regenerator device. Int J Refrig 2018;91:46–54. https://doi.org/10.1016/j.ijrefrig.2018.04.019.

[57] Teyber R, Trevizoli PV, Niknia I, Christiaanse TV, Govindappa P, Rowe A. Experimental performance investigation of an active magnetic regenerator subject to different fluid flow waveforms. Int J Refrig 2017;74:36–44. https://doi.org/10.1016/j.ijrefrig.2016.10.001.

[58] Plaznik U, Tušek J, Kitanovski A, Poredoš A. Numerical and experimental analyses of different magnetic thermodynamic cycles with an active magnetic regenerator. Appl Therm Eng 2013;59:52–9. https://doi.org/10.1016/j.applthermaleng.2013.05.019.

[59] Vieira BP, Bez HN, dos Santos D, Lozano JA, Barbosa JR. Interrelationship between flow profiles and the magnetic waveform and their influence on the performance of first-order active magnetic regenerators. Appl Therm Eng 2023;219:119581. https://doi.org/10.1016/j.applthermaleng.2022.119581.

[60] Nakashima ATD, Dutra SL, Trevizoli PV, Barbosa JR. Influence of the flow rate waveform and mass imbalance on the performance of active magnetic regenerators. Part I: experimental analysis. Int J Refrig 2018;93:236–48. https://doi.org/10.1016/j.ijrefrig.2018.07.004.

[61] Lozano JA, Capovilla MS, Trevizoli PV, Engelbrecht K, Bahl CRH, Barbosa JR. Development of a novel rotary magnetic refrigerator. Int J Refrig 2016;68:187–97. https://doi.org/10.1016/j.ijrefrig.2016.04.005.
[62] Peixer GF, Silva MCR, Lorenzoni A, Hoffmann G, dos Santos D, do Rosário GM, et al. A magnetocaloric air-conditioning system prototype. Int J Refrig 2023;151:1–13. https://doi.org/10.1016/j.ijrefrig.2023.03.014.
[63] Masche M, Liang J, Dall'Olio S, Engelbrecht K, Bahl CRH. Performance analysis of a high-efficiency multi-bed active magnetic regenerator device. Appl Therm Eng 2021;199:117569. https://doi.org/10.1016/j.applthermaleng.2021.117569.
[64] Nakashima ATD, Fortkamp FP, de Sá NM, dos Santos VMA, Hoffmann G, Peixer GF, et al. A magnetic wine cooler prototype. Int J Refrig 2021;122:110–21. https://doi.org/10.1016/j.ijrefrig.2020.11.015.
[65] Lionte S, Risser M, Vasile C, Elouad L, Muller C. Adapting an active magnetic regenerator to a continuous fluid flow application. Int J Refrig 2018;85:303–13. https://doi.org/10.1016/j.ijrefrig.2017.10.009.
[66] Huang B, Lai JW, Zeng DC, Zheng ZG, Harrison B, Oort A, et al. Development of an experimental rotary magnetic refrigerator prototype. Int J Refrig 2019;104:42–50. https://doi.org/10.1016/j.ijrefrig.2019.04.029.
[67] Dall'Olio S, Masche M, Liang J, Insinga AR, Eriksen D, Bjørk R, et al. Novel design of a high efficiency multi-bed active magnetic regenerator heat pump. Int J Refrig 2021;132:243–54. https://doi.org/10.1016/j.ijrefrig.2021.09.007.
[68] Coleman HW, Steele WG. Uncertainty Analysis for Engineers Uncertainty Analysis for Engineers 2018.
[69] Lozano JA. Designing a rotary magnetic refrigerator (PhD thesis) 2015.
[70] de Oliveira PM. On air-water two-phase flows in return bends. 2013. p. 155.
[71] Lei T. Modeling of active magnetic regenerators and experimental investigation of passive regenerators with oscillating flow. Technical University of Denmark; 2016.
[72] Liang J, Nielsen KK, Engelbrecht K, Bahl CRH. Heat transfer figures of merit for mapping passive regenerator performance to active regenerator cooling power. Appl Therm Eng 2020;181:115993. https://doi.org/10.1016/j.applthermaleng.2020.115993.
[73] Engelbrecht K, Bahl CRH. Evaluating the effect of magnetocaloric properties on magnetic refrigeration performance. J Appl Phys 2010. https://doi.org/10.1063/1.3525647.
[74] Vieira BP, Bez HN, Kuepferling M, Rosa MA, Schafer D, Plá Cid CC, et al. Magnetocaloric properties of spheroidal La(Fe,Mn,Si)13Hy granules and their performance in epoxy-bonded active magnetic regenerators. Appl Therm Eng 2021;183:116185. https://doi.org/10.1016/j.applthermaleng.2020.116185.
[75] Aguilera JJ, Meesenburg W, Markussen WB, Zühlsdorf B, Elmegaard B. Real-time monitoring and optimization of a large-scale heat pump prone to fouling - towards a digital twin framework. Appl Energy 2024;365:123274. https://doi.org/10.1016/j.apenergy.2024.123274.
[76] Almeida-Trasvina F, Smith R, Jobson M. Development of an energy-efficient single mixed refrigerant cycle for small-scale LNG production. Ind Eng Chem Res 2021;60:12049–67. https://doi.org/10.1021/acs.iecr.1c00432.
[77] Govindappa P, Trevizoli PV, Niknia I, Christiaanse TV, Teyber R, Rowe A. Experimental characterization of multilayer active magnetic regenerators using first order materials: multiple points of equilibrium. J Appl Phys 2018;124. https://doi.org/10.1063/1.5040491.
[78] Lei T, Engelbrecht K, Nielsen KK, Neves Bez H, Bahl CRH. Study of multi-layer active magnetic regenerators using magnetocaloric materials with first and second order phase transition. J Phys D Appl Phys 2016;49. https://doi.org/10.1088/0022-3727/49/34/345001.
[79] Pineda Quijano D, Infante Ferreira C, Brück E. Layering strategies for active magnetocaloric regenerators using MnFePSi for heat pump applications. Appl Therm Eng 2023;232:120962. https://doi.org/10.1016/j.applthermaleng.2023.120962.